

Illumination and Noise-Based Scene Classification - Application to SAR Sea Ice Imagery

by

Namrata Bandekar

A thesis
presented to the University of Waterloo
in fulfillment of the
thesis requirement for the degree of
Master of Applied Science
in
Systems Design Engineering

Waterloo, Ontario, Canada, 2011

© Namrata Bandekar 2011

I hereby declare that I am the sole author of this thesis. This is a true copy of the thesis, including any required final revisions, as accepted by my examiners.

I understand that my thesis may be made electronically available to the public.

Abstract

Spatial intensity variation introduced by illumination changes is a challenging problem for image segmentation and classification. Many techniques have been proposed which focus on removing this illumination variation by estimating or modelling it. There is limited research on developing an illumination invariant classification technique which does not use any preprocessing.

A major focus of this research is on automatically classifying synthetic aperture radar (SAR) images. These are large satellite images which pose many challenges for image classification including the incidence angle effect which is a strong illumination variation across the image. Mapping of full scene satellite images of sea-ice is important for navigational purposes for ships and also for climate research. The images obtained from the RADARSAT-2 satellite are dual band, high quality images. Currently, sea ice chart are produced manually by ice analysts at the Canadian Ice Service. However, this process can be automated to reduce processing time and obtain more detailed pixel-level ice maps. An automated classification algorithm to achieve sea ice and open water separation will greatly help the ice analyst by providing sufficient guidance in the initial stages of creating an ice map. It would also help the analyst to improve the accuracy while finding ice concentrations and remove subjective bias.

The existing Iterative Region Growing by Semantics (IRGS) algorithm is not effective for full scene segmentation because of the incidence angle effect. This research proposes a "glocal" (global as well as local) approach to solve this problem. The image is divided in a rectangular grid and each rectangle is segmented using IRGS. This is viewed as an over-segmentation of the original image. Finally, IRGS is used globally to glue together the over-segmented regions. This method yields acceptable results with the denoised images. The proposed technique can also be used for general image classification purposes. Extensive testing was done to investigate the best set of parameters for the proposed approach. Images were simulated with the SAR illumination variation and multiplicative speckle noise. The technique was effective for general classification and attained accurate results for full scene SAR segmentation.

Acknowledgements

I would like to thank my supervisor, Prof. David Clausi, for the guidance and support he has provided throughout this work. I would also like to thank my readers Prof. Maud Gorbet and Prof. Alex Wong for reviewing this thesis. I am grateful to Peter Yu for his assistance in making me familiar with the existing algorithms and code base. I would also like to thank Fan Li for his help in finding the relationship between processing time and image size for the existing methods.

The RADARSAT images used in this thesis are provided by the Canadian Ice Service (CIS) and are copyrighted by the Canadian Space Service. I acknowledge the assistance of Matt Arkett and Angela Chan at CIS for making the images available to me.

Table of Contents

List of Tables	vii
List of Figures	viii
1 Introduction	1
2 Background	3
2.1 SAR Overview	3
2.2 Feature Extraction	8
2.3 Classification Techniques	9
2.3.1 Supervised Classification Methods	10
2.3.2 Unsupervised Classification Methods	10
2.4 Thesis Objectives	12
3 Methods	14
3.1 Existing Methods	14
3.2 Automatic Polygon Definition and Classification	16
3.3 Data Generation	19
3.3.1 Modeling the SAR Noise and Illumination Variation	19
3.3.2 Test Protocol	21

4	Testing and Results for Colour and Grayscale Images	23
4.1	Data	23
4.2	Tests and Results	24
4.2.1	Grayscale Images	24
4.2.2	Colour Image	30
5	Testing and Results for Texture Images	34
5.1	Data	34
5.2	Tests and Results	36
6	Testing and Results for SAR Images	39
6.1	Data	39
6.2	Tests and Results	44
7	Conclusion and Future Work Recommendations	59
7.1	Summary	59
7.2	Future Work Recommendations	61
	APPENDICES	64
A	Additional Statistics for the Classification Tests	65
A.1	Performance Measures for Grayscale Images	65
A.2	Performance Measures for Colour Images	68
A.3	Performance Measures for Texture Images	69
B	Matlab codes	70
	References	74

List of Tables

3.1	GRSR coefficients	19
4.1	Accuracy results for triangle grey image.	25
4.2	Accuracy results for four band grey image.	30
4.3	Accuracy results for triangle colour image.	32
5.1	Accuracy results for texture image.	37
A.1	Sensitivity results for triangle grey image.	65
A.2	Specificity results for triangle grey image.	66
A.3	Sensitivity results for four band grey image.	66
A.4	Specificity results for four band grey image.	67
A.5	Sensitivity results for triangle colour image.	68
A.6	Specificity results for triangle colour image.	68
A.7	Sensitivity results for texture image.	69
A.8	Specificity results for texture image.	69

List of Figures

2.1	Geometry of the SAR image acquisition system.	4
2.2	Incidence angle effect	7
2.3	Test results for K-means and IRGS.	12
3.1	Major steps in the IRGS algorithm.	15
3.2	Major steps in the Glocal algorithm.	17
4.1	Grayscale test images.	23
4.2	Triangle colour image (378x380).	24
4.3	Results for Triangle grey test image.	25
4.4	Accuracy plot for triangle grey image.	26
4.5	Blocky artefacts observed in classification results caused by a poor placement of polygons.	27
4.6	Results for four band grey image.	28
4.7	Accuracy plot for four band grayscale image.	29
4.8	Triangle colour image results.	31
4.9	Results for triangle colour image at illumination level 3.	32
4.10	Accuracy plot for triangle colour image.	33
5.1	Texture test image (512x512).	35
5.2	Test results for texture image at illumination level 6.	36
5.3	Texture image accuracy plot.	37

5.4	Test results for texture image at illumination level 7.	38
6.1	Cropped SAR test image for the HH band (1494x805).	40
6.2	RADARSAT-2 Image taken on April 01, 2010 (10487x9620 pixels).	41
6.3	RADARSAT-2 Image (10557x10114 pixels).	43
6.4	Wormy appearance of the HH and HV bands (scale 1:1).	44
6.5	Full scene classification.	45
6.6	Different stages of the Glocal approach.	46
6.7	Glocal results for HH and HV bands.	48
6.8	HH,HV Glocal result for Figure 6.3 for polygon size 128. The strong illumination in HH throws off the algorithm. Blocky artefacts are introduced. . .	49
6.9	Result of the Glocal method for polygon size 512 applied to HH and HV bands.	50
6.10	Result of the Glocal approach applied to the dual band SAR.	51
6.11	Global result for HV band.	52
6.12	Relationship between processing time and image size for Global and Glocal methods.	54
6.13	SAR Test results.	56
6.14	Result obtained by changing gluing parameters.	58
7.1	Removing blocky artefacts by moving the grid.	62

Chapter 1

Introduction

In image segmentation and classification, spatial variation in intensities across homogeneous regions or illumination changes is a challenging problem [1]. In this research, we will focus on developing a robust image classification method which is not sensitive to illumination variation.

Another area of focus for this thesis is solving this problem for large images. Large images such as synthetic aperture radar (SAR) images are non-stationary. There is considerable variation within a class, especially, if it is distributed throughout the image. There is variation within the same scene and from scene to scene. The same ice type can appear different in different seasons and locations. Also, there is ambiguity in transition areas to another ice type. These images also pose another challenge, which is, dealing with speckle noise. The multiplicative speckle noise present in the image makes it hard to extract the tone and texture of the image. The illumination invariant classification method should also work in the presence of speckle noise. Another aspect of this problem is the processing speed for large images. This is not a research goal for this thesis but will be discussed briefly later.

The illumination variation arises from the incidence angle effect in SAR imagery. This effect makes it difficult to distinguish between open water and ice. Although we focus on developing an algorithm which can overcome SAR spatial intensity variations, it can also be used with any other illumination model where the illumination changes gradually.

SAR sea ice charts are maps of regions in the sea with ice presence. These maps provide detailed information about the presence of various types of ice, their thickness, size and concentration in these regions. Monitoring sea-ice is necessary for both operational and scientific activities such as ship navigation and climate research.

Automating the sea-ice mapping process would remove subjective bias and increase accuracy. Some applications, such as environmental research, need pixel level ice maps which can provide greater detail. Everyday, there is a large volume of data to be processed as the satellite data is received constantly. An automated sea ice segmentation algorithm would also facilitate the entire process by decreasing throughput time. The Iterative Region Growing using Semantics (IRGS) algorithm was developed for this purpose [2], [3]. However, IRGS is not very effective for segmenting images with illumination changes. The new classification method would play a pivotal role in SAR sea ice segmentation and classification. Sea ice and open water discrimination for SAR images is crucial to provide an accurate estimate of the concentrations of ice and water in a given region. An automated algorithm to achieve this separation will greatly help the ice analyst by providing sufficient guidance in the initial stages of creating an ice map. It would also help the analyst to improve the accuracy of estimation while finding ice concentrations.

Chapter 2 presents an overview of the SAR imaging system. It also discusses the state of the art classification techniques for sea ice and a few illumination robust segmentation methods. An initial evaluation of the IRGS algorithm and K-means clustering is presented for images with illumination variation to develop a set of research goals that the method proposed in this thesis will address. The existing IRGS algorithm and the proposed method is explained in Chapter 3. The performance of the proposed algorithm is evaluated through several experiments presented in Chapters 4, 5 and 6. Finally, the major research conclusions are discussed in Chapter 7 and the thesis objectives are revisited. Chapter 7 also proposes several lines of future improvement.

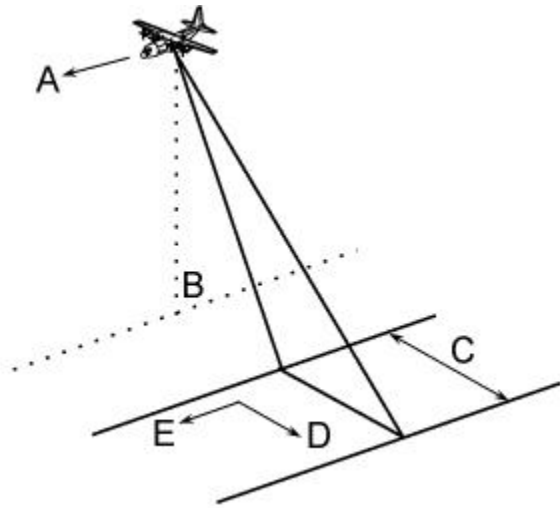
Chapter 2

Background

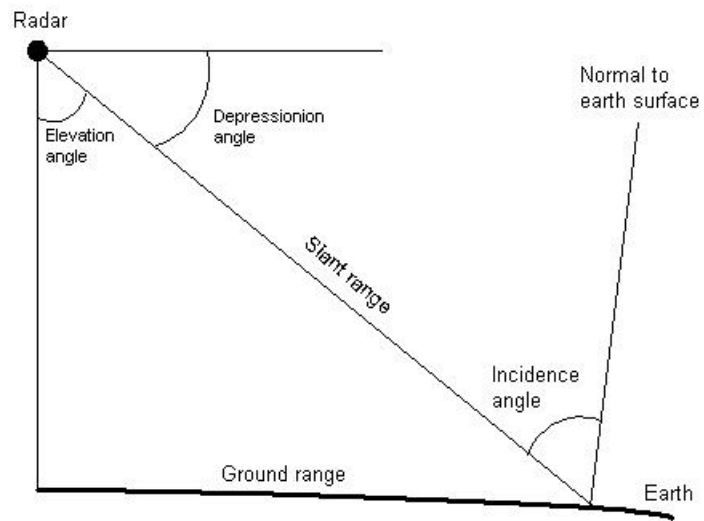
2.1 SAR Overview

The geometric configuration of a satellite is shown in Figure 2.1(a). The satellite carries a sensor equipment which sends out electromagnetic waves perpendicular to the direction of the flight. These pulses are sent at periodic intervals. The direction of motion of the spacecraft is known as the azimuth and the direction perpendicular to the flight direction is called the range. The receiving antenna receives a reflected wave which is the backscatter from the earth's surface.

In the side-looking viewing geometry, shown in Figure 2.1(a), the nadir (B) is located directly below the imaging platform. The microwave beam is transmitted perpendicular to the direction of flight (A) in an oblique plane illuminating the swath (C). Azimuth (E) is the along track axis parallel to the flight direction while range (D) is the axis perpendicular to the flight direction. The portion of the image swath nearest to the nadir is called the near range while the points on the ground in the swath farthest away from the nadir are called far range. The incidence angle, as shown in Figure 2.1(b), increases from near range to far range. The radial line of sight distance between the radar and a point on the surface is called the slant range distance, illustrated in Figure 2.1(b). The ground range distance is the true horizontal distance along the ground from the surface point to the nadir.



(a) A SAR image acquisition system.



(b) Parameters for the imaging platform.

Figure 2.1: Geometry of the SAR image acquisition system. Source: [4]

An important parameter of the SAR system is the polarization of pulses emitted by the sensor. These pulses can be either horizontally(H) or vertically(V) polarized. Similarly, the signal received by the satellite can have either type of polarization. Hence, the data captured by a SAR system can be classified into four categories (HH, HV, VH and VV) based on the transmitting and receiving modes. The various polarization modes affect the measurement being obtained as different modes interact in different ways with the surface and lead to a unique backscatter signal. However, the HV and VH bands capture the same information [5].

SAR satellites do not necessarily capture all polarization modes. Based on this SAR satellites are categorised as single band (measures only HH or VV), dual band (measures both HH and HV) and quad band (measures all four channels). The RADARSAT-I satellite captures only the HH band, ERS-1 and 2 capture only the VV band and some RADARSAT satellites which have high resolution modes can capture all four polarizations.

Various effects are observed in SAR imagery due to the operating environment of the sensor as well as the ground conditions. Speckle noise is caused when coherent light is reflected from a rough surface. Rough surfaces have multiple points of reflection for the coherent pulse. This causes a constructive and destructive interference between the reflected waves. Because of this, the grey level at a pixel can be very different from its neighbouring pixel. SAR images have a grainy appearance due to the presence of speckle noise. This noise is also known to be multiplicative, that is, it depends on the grey level of the backscattered signal [6]. There have been many attempts in the literature to model SAR noise [7], [8].

The incidence angle effect can be observed in wide swath images when there is a considerable difference between the incidence angle at near range and far range as shown in Figure 2.1(a). The incidence angle can vary between 20 and 50 degrees in Scan SAR Wide images. The backscatter from a surface is dependent on the incidence angle and the wind speed on that surface [9]. The brightness at a point decreases with the increase in the incidence angle at that point. The surface behaves like a mirror for larger incidence angles reflecting all the energy that it receives away from the sensor. However, it increases with increase in the wind speed as larger wind speed makes the surface rougher causing the signal to be backscattered from multiple points. Hence, it makes the open water look much brighter than its SAR signature. This complex relationship is modelled by Shokr [9]. This effect can lead to open water being misclassified as ice as shown in Figure 2.2 (c). The incidence angle effect can be seen more prominently in the HH channel as shown in Figure 2.2 (a). Most of the energy which is sent by the sensor is reflected back with the same polarization. Hence, this effect can be seen more prominently in HH. It is present in the HV band but to a far lesser extent. A strong banding effect can be seen in the HV band.

This may be related to the signal to noise ratio varying across the image as observed in ENVISAT ASAR experiments [10]. The effect is illustrated in Figure 2.2 (b).

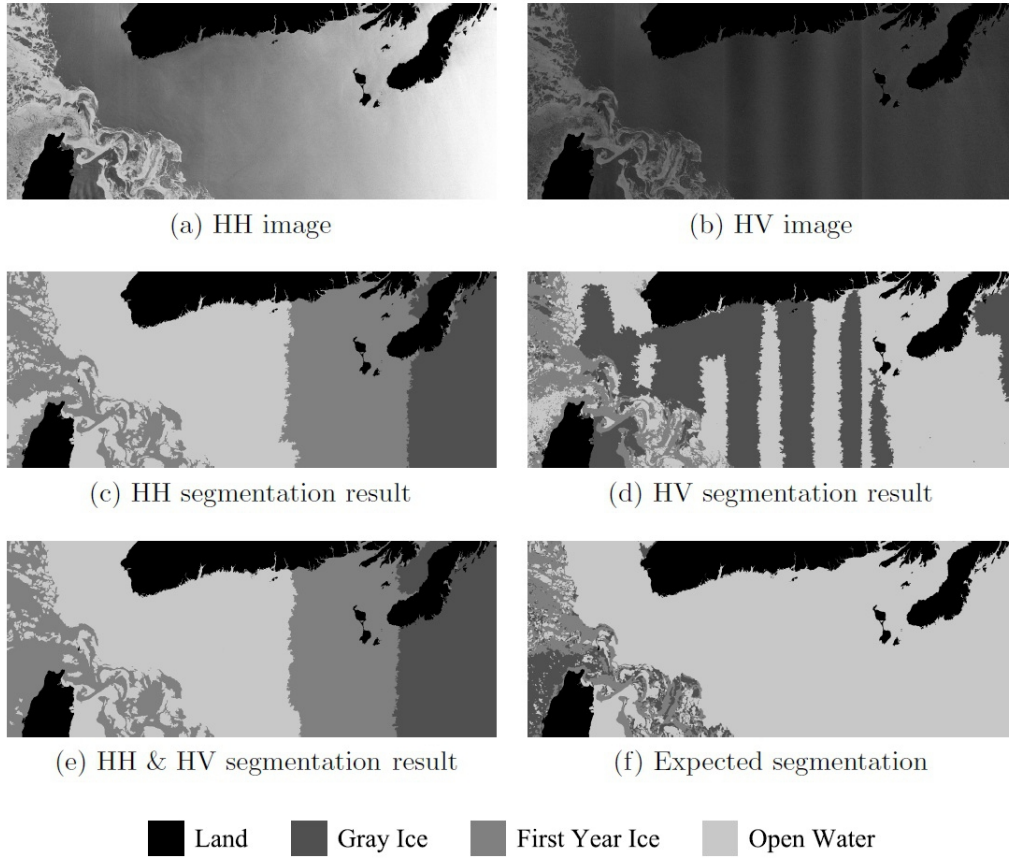


Figure 2.2: Image illustrating incidence angle effect in the horizontal (HH) band and banding effect in the vertical (HV) band and their impact on IRGS classification results.

The environmental conditions have a big impact on the appearance of different ice types and open water. Ice which is covered with water cannot be distinguished clearly and can be tricky to identify even for an sea ice analyst. Other conditions like temperature, salinity, existence of snow cover and intrusion of sea water also affect the radar signature of ice [11].

2.2 Feature Extraction

The classification algorithm should be robust to the effects caused by the sensor and the ground conditions. All classification algorithms rely on different features of a class to identify regions belonging to that class. Features are statistical characteristics which distinguish different classes. Various feature measures can be of interest for a classification algorithm based on the type of image data. For SAR images, backscatter or the raw grey levels in the different polarization bands (HH and HV) can be used. The colour channels are used as features for colour images based on the colour space in which the image information is represented the best. For texture images such as Brodatz dataset [12], the most commonly used texture features are grey Level Co-occurrence Matrix [13] (GLCM) and Gabor features [14].

Various statistical measures have been applied for classification ranging from backscatter intensity to first order statistics such as mean, variance etc. [15], [16]. Autocorrelation as a texture measure is not very sensitive to wave conditions. Karvonen investigates the effectiveness of autocorrelation in distinguishing open water from ice [15]. However, the method uses a segmentation algorithm which pre-processes the image to remove the incidence angle effect. Local thresholding has been used to solve the backscatter incidence angle dependence problem [17]. The method uses wavelet coefficients as a texture measure and different thresholds at different incidence angles to classify open water from sea ice. Segment-wise edge statistics are used to determine the classification in [18]. The image is first pre-processed to incorporate incidence angle correction and edge-preserving speckle filtering. The image is then segmented. The edges in the resulting image are classified as either segment edges or boundaries. The boundary edges help in extracting the shape and within-segment edge features give more information about the ice properties. Soh observed that GLCM texture features can be effective in segmenting sea ice [16] if the various parameters such as quantization levels of the image, displacement and orientation values are defined optimally. Clausi *et al.* noted that varying the quantization level for GLCM does not have any effect on the classification [19] because a few co-occurrence features perform better at coarser quantization levels while others show better results for finer quantization.

Augmenting the GLCM features with Markov random fields seemed to produce the best feature set [19].

2.3 Classification Techniques

Various methods for classifying sea ice have been studied in the literature. A comment should be made concerning the distinction between classification and segmentation methods. Segmentation can be defined as partitioning the image into homogeneous regions, whereas classification refers to correctly identifying each of these homogeneous regions as belonging to a certain class, where the classes are agreed upon in advance. So, if the regions belonging to the same class are spatially isolated, segmentation would not associate them but classification would. A classification algorithm implicitly segments an image.

Classification methods can be categorised as either supervised and unsupervised or pixel-based and region-based. Several classification methods, both pixel-based and region-based, have been studied. The region-based techniques are observed to be more effective. The pixel-based methods rely on low level features such as tone and texture extracted from the image. If the image has spatial intensity variations and noise like SAR images, these features will also be highly variable. A region-based technique considers more stable features which depend on the pixel and its neighbours. Hence, they are less sensitive to noise and inhomogeneity [20], [21]. Another way of categorising these classification techniques is to partition them into labelled and unlabelled methods. Labelled techniques are associated with a supervised process to label each of the classified regions with the true class label whereas unlabelled methods employ an unsupervised process which does not associate the classes with their labels.

Both supervised and unsupervised methods have been studied in great detail in the literature. Supervised methods use knowledge of class distributions to classify each pixel into an ice type. Prior knowledge of class distributions of low level features and training is required. However, these features can vary widely based on the sensor environment, location and season. In unsupervised techniques, the pixels are grouped first according to some similarity or dissimilarity measure and then classified to obtain the segmentation. Unsupervised methods do not need any prior information or training. We discuss some of the methods below.

2.3.1 Supervised Classification Methods

Karvonen and Simila proposed a Pulse Coupled Neural Network (PCNN) based algorithm for sea ice segmentation and classification in the Baltic Sea [22]. They use a two scale algorithm which combines an artificial neural network with some expert system like rules. Other supervised methods, such as the one proposed by Haarpaintner and Solbo, use a flood mapping algorithm [23]. However, prior to applying this algorithm the image needs to be sliced along the range direction according to the incidence angle to overcome the strong illumination variation. The Advanced Reasoning using Knowledge for Typing of Sea ice (ARKTOS) [24] is another supervised classification method. It mimics the reasoning process of sea-ice expert analysts by forming system rules. It also uses multi-sourced data fusion to obtain more information of the scene.

Supervised methods are more often very complex and computationally expensive. They are also less efficient as a lot of expertise is needed to pick out training samples. The non-stationarity of classes in big SAR images is another major reason why these methods would not work well on sea ice data. The same ice type can appear different in different seasons and locations. There is also variation in transition areas between different ice types. Finally, supervised methods would never be adopted for operational SAR sea ice image recognition since the training stage is time consuming and the process suffers from human bias.

2.3.2 Unsupervised Classification Methods

The IRGS algorithm proposed by Yu and Clausi [2] utilizes a Markov Random Field (MRF) based formulation for image segmentation. It is based on two main principles of aggregating regions. It merges two regions if they are statistically similar or if they have a low edge strength between them. Wu *et al.* propose a sea-ice image segmentation method which utilizes a non-Gaussian triplet Markov field (TMF) model combined with the edge penalty principle [25]. To optimize the objective function obtained from the energy formulation of the TMF system, an iterative multi-region merging Bayesian maximum posterior mode algorithm is used. The edge penalty prevents segments from smoothing across boundaries during this region merging step.

A hierarchical step-wise optimization (HSWO) algorithm is proposed by Carvalho *et al.*, which uses a segmentation technique similar to that of IRGS [26]. The raw noisy image is first over-segmented which can be done using the watershed algorithm [27]. The method then applies a region growing technique based on a similarity rule, which employs the

coefficient of variation. This initial region aggregation is followed by an iterative statistical region growing step. A cost function is formed between every pair of adjacent regions based on the boundary strength. The regions with the minimum cost are merged only if they satisfy the Kolmogorov-Smirnov test, that is, the distance between the distributions of the two regions is less than a certain threshold. Dawoud and Netchaev propose an image segmentation method [28] which fuses edge information with IRGS, which is an MRF image segmentation algorithm. A canny edge detector is used and the resulting edge lines are fused with the watershed lines in the image segmentation method. This helps in preserving object contours during the region growing step yielding a more accurate segmentation result.

However, the unsupervised methods described above would not work well on images with illumination variation. A majority of the methods employ look up tables for incidence angle correction [29]. Illumination subtraction using incidence angle correction is a chicken and egg problem. It is not possible to correct a scene for the incidence angle effect because the correction factor is dependent on the type of ice present in that region in the image, which is not known beforehand. To the author's knowledge, there is no known method which is robust to the incidence angle effect in ScanSAR Wide imagery.

There are several methods which pre-process the image for removing noise and other artefacts. Pre-processing steps such as denoising using speckle filters distort the texture measures and blur the boundaries between regions. There has been some research in modelling the luminance channel in images which have inhomogeneous illumination variation [30], [31], [32]. However, these methods do not consider any noise in the illumination models. Moreover, they are computationally expensive and not suitable for large images. This limits their practical applications.

We investigate the performance of IRGS and K-means clustering for images with illumination variation and speckle noise. The generation of these images is presented in detail in Section 3.3. Two experiments were performed, the first one uses an image with only illumination variation and the second one tests the algorithms for both illumination variation and speckle noise. The results of both the tests are shown in Figure 2.3. IRGS is observed to perform better than K-means because in addition to the statistics of the class it also incorporates the spatial context of the pixels which helps in the region growing step. The watershed step in IRGS minimizes the effect of speckle noise for any classification. Watershed breaks up the image into small homogeneous regions. Instead of calculating feature vectors for each pixel for the classification, they are averaged over the entire region which reduces the impact of speckle on these features and hence the classification result. However, IRGS starts failing for a larger illumination gradient as well. This gives context for the next section where the research goals for this thesis are discussed.

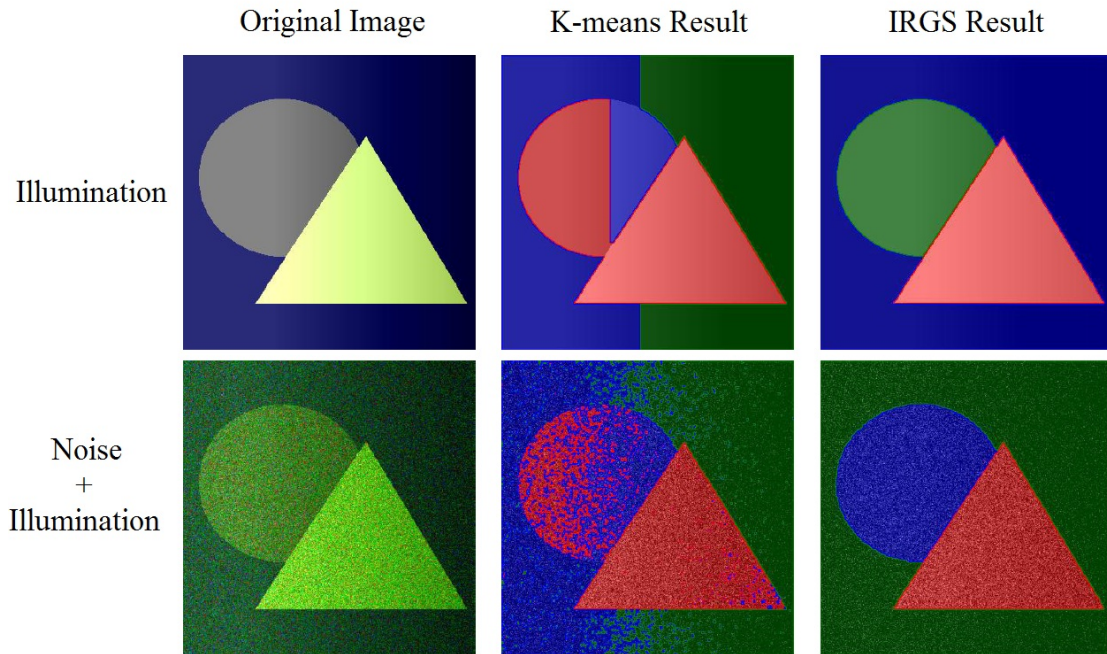


Figure 2.3: Test results for K-means and IRGS.

2.4 Thesis Objectives

This section focuses on clearly identifying the research objectives for this thesis. They are formulated based on the observations in this chapter. Each of the questions is described below with discussions on how these questions will be addressed in the following chapters.

1. How can we overcome spatial illumination variation in images, for the purpose of image classification, regardless of the illumination model?

A two step hierarchical process which first segments small regions of the image locally and then glues the local segmentation results will be implemented. This approach would be less sensitive to within class variations as compared to processing the full SAR scene, all at once, because the variation in a class within a local region will be

less compared to the variations in the class across the whole scene. In the global aggregation step, the class statistics will be averaged over a bigger area which would give more room for larger variations and more importance will be given to edge strength. This method has been described in more detail in Chapter 3.

2. Can this method be applied to process large images like SAR sea ice images efficiently?

IRGS scales exponentially with the size of the region to be segmented [2]. In the first step of the proposed method, only small regions will be segmented. Hence, the algorithm would have a linear time complexity for the number of regions in which the image is partitioned. The second step of the hierarchical process would then just merge the previously formed larger regions with IRGS. This question will be analysed in more detail in chapter 7.

3. What would be the best set of parameters for this approach?

We focus on finding the sensitivity of the algorithm to the polygon size chosen. It is expected that the larger polygon sizes would have the same disadvantages as applying IRGS on the full scene. It would be more sensitive to illumination variations and would take longer to converge to a solution. On the other hand, for very small polygon sizes, the algorithm is expected to yield similar results as IRGS on the full scene. This is because the small segmented regions are finally glued using IRGS globally on all the regions. Using a very small polygon size would be computationally more expensive since IRGS will have to glue a large number of regions in the second step of the hierarchical process. A test protocol will be developed and test images with varying amounts of illumination will be generated to analyze the performance of the algorithm. Chapters 4, 5 and 6 describe more about the testing and results of the proposed approach.

Chapter 3

Methods

This chapter describes both the existing and the proposed methods in greater detail. Section 3.1 presents an explanation of the IRGS algorithm. The proposed method is discussed in Section 3.2. The algorithm seeks to improve the full scene segmentation of sea ice and deal with the incidence angle effect. Section 3.3 describes the test data simulation and experimental protocol that will be used to analyze the performance of the proposed method.

3.1 Existing Methods

This section will focus on explaining the IRGS algorithm mentioned before in Section 2.3.2. This section only gives a brief overview of the algorithm which is described in more detail in [2] and [3].

The algorithm starts out with calculating the image gradient to apply watershed on the entire image as illustrated in Figure 3.1 1(a). IRGS uses a vector field gradient approach (VFG) for calculating the gradient of the image across all channels [33]. This forms small regions and a Region Adjacency Graph (RAG) is created where the nodes are the regions and the boundaries between them form the edges.

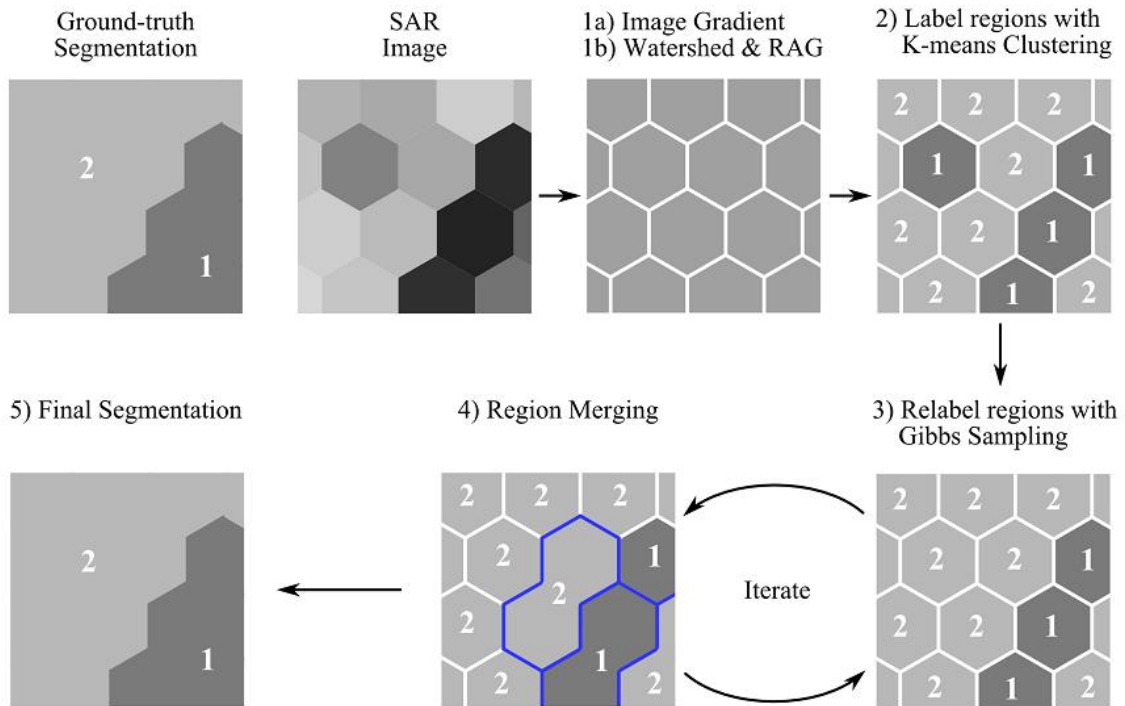


Figure 3.1: Major steps in the IRGS algorithm. IRGS starts by computing the 1a) image gradient to calculate the 1b) watershed regions and form a RAG. An initial labelling is found based on 2)K-means clustering. An iterative optimization process is used thereon where 3) Gibbs sampling is used to find optimal labels and is followed by 4) region merging until the desired number of iterations is reached. 5) A final classification is then obtained. Source: [11]

An initial labelling step is then performed on these regions using K-means clustering. This step is unaffected by speckle noise as the feature vectors used in K-means are averaged over the entire region. To obtain the optimal labelling, the algorithm uses an iterative approach based on two main criteria.

- Regions with similar statistical properties are more likely to belong to the same class.
- Adjacent regions can be classified as belonging to the same class if they have a weak edge between them.

Gibbs sampling [34] is used as the optimization algorithm for finding the optimal label for each node in the RAG. A greedy region merging technique grows the regions which are adjacent to each other into a single region as long the total energy of the system decreases. The Gibbs sampling step is repeated again and this process is carried out iteratively until the user-defined number of iterations is reached.

3.2 Automatic Polygon Definition and Classification

The IRGS method works well for very little variation within the same class. It tends to fail when regions belonging to the same class are spatially isolated and show variation in a few statistical properties. This is mainly because the algorithm gives more priority to the Gaussian statistics of different regions initially while merging and relies on edge strength later on in the iterative step. More specifically, any classification algorithm that uses backscatter (grey level) as a feature will fail under varying illumination conditions.

We describe a novel automatic polygon definition and classification method in this section. Steps for this algorithm are illustrated in Figure 3.2 and detailed below.

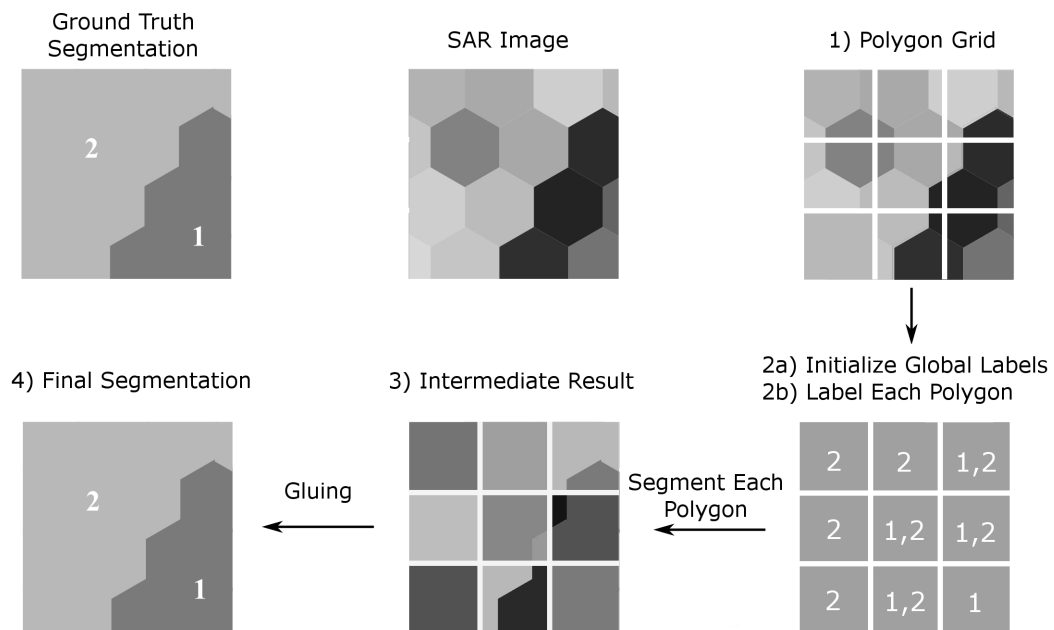


Figure 3.2: Major steps in the Glocal algorithm. 1) A polygon grid is generated based on the optimal polygon size. 2 a) Global labels for the entire image are initialized followed by automatic labelling of each polygon in 2 b). Each polygon can be assigned its true labels if the ground truth classification is known. 3) IRGS is applied on each individual polygon to yield an intermediate result. 4) A final classification is then obtained by gluing all the regions with IRGS.

- **Step 1:** A rectangular grid is formed on top of the image which divides the image into many sub-regions called polygons. In SAR terminology, a polygon is a large region with a mixture of different ice types, each having a significant concentration in the region. Here, each of the rectangles is called a polygon to be consistent with the terminology. Since the polygon grid is generated automatically based on the user desired polygon size, this step is called the "Autopolygon" process. The testing regarding optimal polygon size is discussed in the chapters 4, 5 and 6. The polygon grid is illustrated in Figure 3.2, where the image is divided into a 3x3 grid.
- **Step 2:** The next step is to initialize global labels and classes for the full scene. Each of the polygons is then assigned classes from the global label list. Ideally, if the ground truth for the image exists, then each polygon is assigned the true labels for that region by manually or automatically going through the grid. However, since there is no image validation data for the SAR images provided by CIS and MDA, the true labels for each polygon are unknown. Hence a polygon is assigned the same classes as the full scene. This technique also gives us a fully automated method for ice and open water classification. Figure 3.2 2(a),2(b) demonstrates this process, where each polygon is labelled with the true classes present in that region.
- **Step 3:** Once the labels for each polygon are set, they can be processed individually to yield local classification results. An intermediate result, shown in Figure 3.2, is obtained by employing IRGS to segment the individual polygons.
- **Step 4:** The final step involves merging the results from the preprocessing stage to yield the full scene segmentation of the entire image. Several methods were investigated for gluing the preprocessed polygon results together [35]. A RAG was generated from the preprocessed polygon results and the neighbouring nodes were analyzed to determine if they could be merged into a single node. The difference between the different methods investigated was the criterion used to determine the merging of two regions. IRGS was found to perform the best out of all the methods as it incorporated both the statistics of the regions and edge strength between them. Hence, IRGS was used to glue the results of all the polygons together.

This algorithm is also called the "Glocal" approach since the image is first segmented locally and then this intermediate result is merged globally to obtain the final classification result. This two level hierarchical process gives better performance for speed as well.

3.3 Data Generation

To test if the algorithm could work with images other than SAR a few test images were generated. Illumination was modelled based on SAR incidence angle effect. Speckle noise characteristics followed a Rayleigh distribution [6], [36].

3.3.1 Modeling the SAR Noise and Illumination Variation

The images were modelled for the illumination changes seen in Scan SAR Wide images. The incidence angle varies from 20° to 50°. There are several steps involved in calculating the illumination before including it in the image [37].

The slant range for each ground range point is calculated. Let the image pixels in the range direction be denoted by j , where j is calculated from the start of the range line from the near range to the far range. The ground range to slant range coefficients (GRSR) are fixed for the ScanSAR Wide product [37]. There are six coefficients associated with the conversion and they are tabulated in Table 3.1.

Table 3.1: Table for GRSR coefficients [37]

Coefficient Number	Coefficient Value
1	836212
2	0.31773
3	6.1828e-007
4	-2.7672e-013
5	-6.6369e-021
6	4.94747e-262

The slant range for the j^{th} pixel is

$$RS_j = \sum_{k=1}^{k=6} GRSR(k) * (j * spacing)^{(k-1)} \quad (3.1)$$

where, $GRSR(k)$ is the k^{th} GRSR coefficient and spacing is the distance between the corresponding ground points in meters (set to 100 for ScanSAR Wide [37]).

The earth's radius r is assumed to be $6.36828e + 006$ m and orbit height h is fixed to 798769 m for all images. To model the incidence angle as a function of range position Equation 3.2 is used [37]. The incidence angle (in radians) for the j^{th} pixel is given by:

$$I_j = \arccos \frac{(h^2 - RS_j^2 + 2.r.h)}{2.RS_j.r} \quad (3.2)$$

The backscatter in dB is calculated based on the data compiled by Shokr [9]. The backscatter is modelled as a function of incidence angle for different wind speeds. For this research, a constant mid range wind speed of 20 m/s is assumed for all images. The backscatter in grey level at the pixel j is then calculated as follows:

$$\text{BackScatter} = \frac{\sigma_0 \cdot (-255)}{\sigma_{MIN}} + 255 + 0.5; \quad (3.3)$$

where σ_0 is the backscatter in dB and σ_{MIN} is set to -25 dB, which is the noise floor. The illumination image is then multiplied with the test image to simulate the intensity variation.

The speckle noise is simulated as a multiplicative noise and follows the model described by Bolter *et al.* [6]. The statistical properties of the speckle noise are described by a Rayleigh probability distribution. The parameters for the Rayleigh distribution were chosen based on the observations described by Lee *et al.* [38]. A speckle noise image having the same dimensions as the test image is generated. The simulated image is then multiplied pixel by pixel with the noise image. To simulate the effect of multiple looks, several speckle noise images are generated where the number of images generated is the same as the number of independent looks. These speckle images were averaged and the resulting noise image was multiplied pixel by pixel with the test image. Adjacent pixels in SAR are not statistically independent. To introduce correlation between neighbouring pixels we employ a simple smoothing filter [6].

The illumination and noise are included in the image together as follows:

$$f(x, y) = \frac{1}{N} \cdot \sum_{j=1}^N \int \int h(x, y, k_1, k_2) \cdot I(k_1, k_2) \cdot l(k_1, k_2) \cdot n_j(k_1, k_2) dk_1 dk_2 + m_j(x, y) \quad (3.4)$$

where h is the point spread function of the smoothing filter, I is the test image, l is the illumination image, n is the noise image, m is the additive white Gaussian noise added to the image to account for the phenomenon which is not addressed by h [39]. The

resulting image is averaged over N looks. The standard deviation for the phenomenon noise distribution is chosen to be 5% of the dynamic range of the test image. To keep the model simple, h is assumed to be stationary or spatially invariant. The dynamic range of the image is adjusted to avoid saturation.

3.3.2 Test Protocol

The maximum dynamic range that could be achieved for the illumination variation was 160 grey levels because of the incidence angle range for ScanSAR Wide images. The illumination was broken down into different levels. The dynamic range of the illumination was varied in steps of 16 grey levels. So illumination level 1 means an illumination gradient with dynamic range 16 was added to the image. For the colour and grayscale images, a much finer scale was developed as the algorithm broke down much faster for these images compared to the texture image. A middle level was added between every two illumination levels. So, an illumination level of 0.5 means that illumination with dynamic range of 8 grey levels was added to the image.

For each image, test images were generated for nine illumination levels. However, based on the results, the performance of the algorithm for only the first five illumination levels is shown, for the colour and grayscale test images with a step size of 0.5. The Brodatz texture image showed much better results. So all the nine illumination levels are shown with a step size of 1. For all the images a constant level of noise was added. Results were obtained by parametric testing for various illumination levels and polygon sizes.

An objective classification accuracy measure was used to measure the performance of the algorithm. Since the measures used were binary classification measures, they were micro-averaged over all the classes to yield a single aggregate measure for each test [40]. Macro-averaging calculates a simple arithmetic average for each performance metric, however micro-averaging pools together all the statistics and computes an effective measure for all the classes. Micro-averaging does not give an equal weight to each class unlike macro-averaging. The micro-averaged accuracy is calculated as

$$Accuracy = \frac{\sum_{i=1}^N (TP_i + TN_i)}{\sum_{i=1}^N (TP_i + TN_i + FP_i + FN_i)} \quad (3.5)$$

where N is the total number of classes, TP_i is the number of correctly classified pixels belonging to class i , TN_i is the number of pixels which are correctly identified as not belonging to class i , FP_i is the number of pixels incorrectly classified as belonging to class i and FN_i is the number of pixels which are incorrectly identified as not belonging to class i .

The correspondence of labels between the ground truth and the result image is determined by finding the label in the result image which matches with maximum number of pixels for a given label in the ground truth. Apart from the accuracy, performance measures such as sensitivity and specificity were also calculated. Sensitivity measures the ability of the classification test to correctly identify positive results whereas specificity indicates the ability of the test to accurately identify negative results. Mathematically, sensitivity of the can be calculated as follows:

$$Sensitivity = \frac{\sum_{i=1}^N TP_i}{\sum_{i=1}^N (TP_i + FN_i)} = \frac{\sum_{i=1}^N C_i}{\text{Total number of pixels in the image}} \quad (3.6)$$

where N is the total number of classes, TP_i , FN_i are defined as discussed above and C_i is the number of correctly classified pixels for class i .

The specificity, on the other hand, is determined according to the following equation.

$$Specificity = \frac{\sum_{i=1}^N TN_i}{\sum_{i=1}^N (TN_i + FP_i)} \quad (3.7)$$

where TN_i is the number of pixels which are correctly identified as not belonging to class i and FP_i is the number of pixels incorrectly classified as belonging to class i .

A pass-fail criterion is also measured. The algorithm is said to fail if it misclassifies more than 50% of a class in an image. All the results which fail with the pass-fail measure are marked with a 'x' and the ones which pass are marked with a 'o'. The 'x's and 'o's are colour coded based on the objective classification accuracy measure. The results with objective accuracies above 0.9 are coloured blue. The ones with accuracy between 0.9 and 0.7 are coloured green and the rest are coloured red. For all tests, the IRGS result for the full image is defined as the "global" result.

Chapter 4

Testing and Results for Colour and Grayscale Images

4.1 Data

Two grey scale images, illustrated in Figure 4.1, were synthetically generated. The image shown in Figure 4.1(a) contains four grey level bands which have grey values 15, 95, 175 and 255. The bands are of varying height so that the polygon boundaries do not fall on a boundary between two classes in the image. The height of the bands from top to bottom is 108, 118, 138 and 148 respectively.



(a) Four band grey image (512x512). (b) Triangle grey image (378x380).

Figure 4.1: Grayscale test images.

The triangle grey image, illustrated in 4.1(b), has been used to test IRGS by Kai *et al.* [3]. The grey level values were modified to 82 for background, 130 for the circle and 190 for

the triangle. This was done to increase the contrast, particularly between the circle and the triangle. The four band grey image was generated as it demonstrates the incidence angle effect on a wide strip of constant grey level. Also, the results would show the sensitivity of the algorithm to the grey levels. Illumination was added to the grayscale images following the model described in Section 3.3. The colour image, shown in Figure 4.2, was also used by Kai *et al.* [3]. Illumination was added to only the Y channel whereas speckle noise was added to all three channels : Y,U and V.

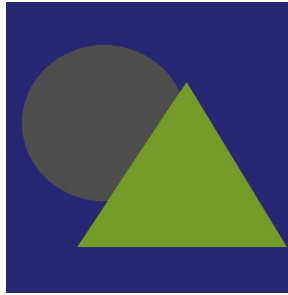


Figure 4.2: Triangle colour image (378x380).

4.2 Tests and Results

As mentioned in Section 3.3.2, images were generated for nine illumination levels with a step size of 0.5.

4.2.1 Grayscale Images

The triangle grey image was tested until illumination level 4. The classification was observed to fail for all polygon sizes above level 2.5, although the objective metric gave an accuracy above 0.6. Hence, the images were only tested until level 4. The size of the polygons was increased by multiples of two from 16 to 256 since the size of the image was 378x380.

The IRGS algorithm, when applied to the full image, fails at level 1.5 but the Glocal approach yields acceptable results until level 2.5 for polygon sizes 32, 64 and 128. Figure 4.3 shows the results for illumination level 1.5. This proves that the Glocal method can handle higher levels of illumination variation.

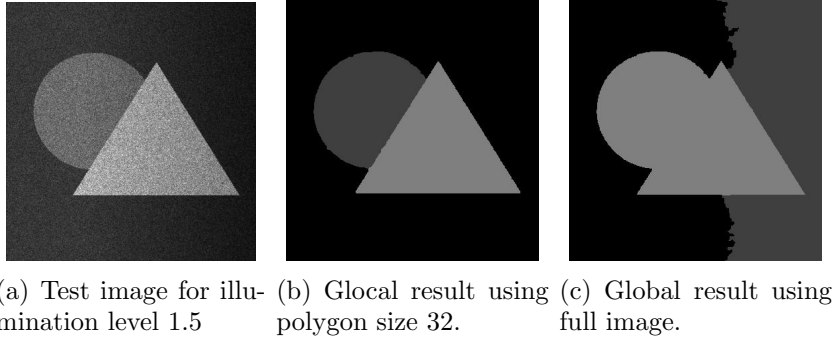


Figure 4.3: Triangle grey test image and results for illumination level 1.5. The global approach (c) fails by breaking the illuminated background into two classes while the Glocal approach (b) is successful.

Polygon size 16 is not successful since the polygons are not given the true class labels. Each polygon is initialised with all three class labels, and hence the results for this size are similar to the global result. The Glocal method failed according to the pass-fail criterion for all polygon sizes after level 2.5 because of low contrast difference between the various classes in the image. Figure 4.4 and Table 4.1 demonstrate these results.

Table 4.1: Accuracy results for triangle grey image.

Illumination level	Glocal Polygon Dimensions (in pixels)				Global
	32x32	64x64	128x128	256x256	
0	0.9997	0.9980	0.9999	0.9998	0.9997
0.5	0.9994	0.9972	0.9997	0.9996	0.9997
1	0.9994	0.9972	0.9996	0.9995	0.9996
1.5	0.6983	0.9969	0.9993	0.9947	0.6957
2	0.6886	0.9969	0.9994	0.9994	0.6827
2.5	0.6831	0.9950	0.9978	0.9976	0.6762
3	0.6801	0.6992	0.6994	0.6996	0.6665
3.5	0.6776	0.6970	0.6993	0.6994	0.6582
4	0.6655	0.6964	0.6991	0.6933	0.6535

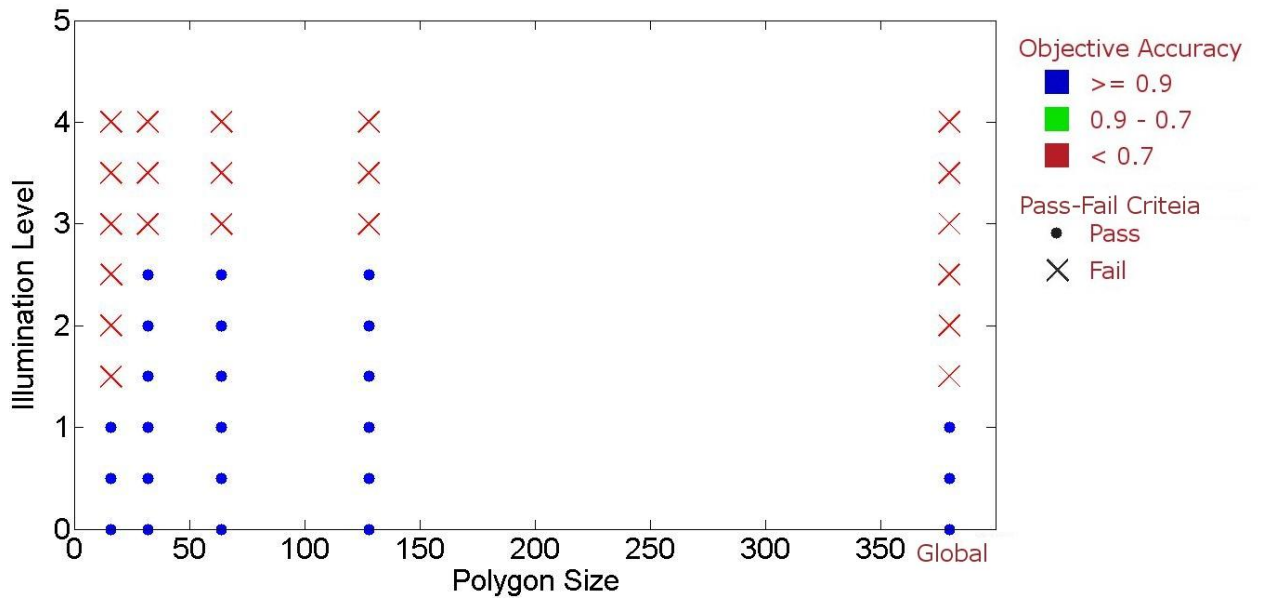
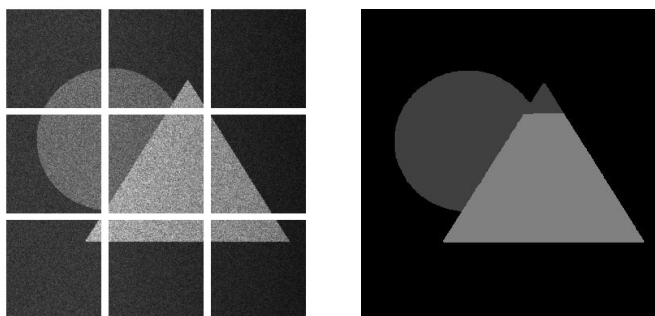


Figure 4.4: Accuracy plot for triangle grayscale test image (Figure 4.1(b)).

The classification was also affected by the position of the polygons. If the polygon had a very small region of one of the classes, then the classification result for that polygon would be blocky. This also introduces blocky artefacts in the glued image as illustrated in Figure 4.5.



(a) Polygon grid for Figure 4.1(b) at illumination level 2. (b) Glocal result for polygon size 128.

Figure 4.5: Blocky artefacts observed in classification results caused by a poor placement of polygons.

The four band grey image was tested until illumination level 4.5 in steps of 0.5. The image has a size of 512x512 pixels, so the polygon size was varied from 32 to 512. The proposed classification algorithm gives accurate results for all polygon sizes until level 2 of illumination. Minor misclassifications can be seen in the global result, as shown in Figure 4.6(f), since the contrast between the third and fourth band is low. Also, the brighter grey levels are more sensitive to the change in illumination causing each class to be classified into separate classes, that is, the contrast of the two lower classes from the right to the left is much higher than the contrast for the top two classes. However, the Glocal approach performs better and yields a near perfect classification as shown in Figure 4.6(e).

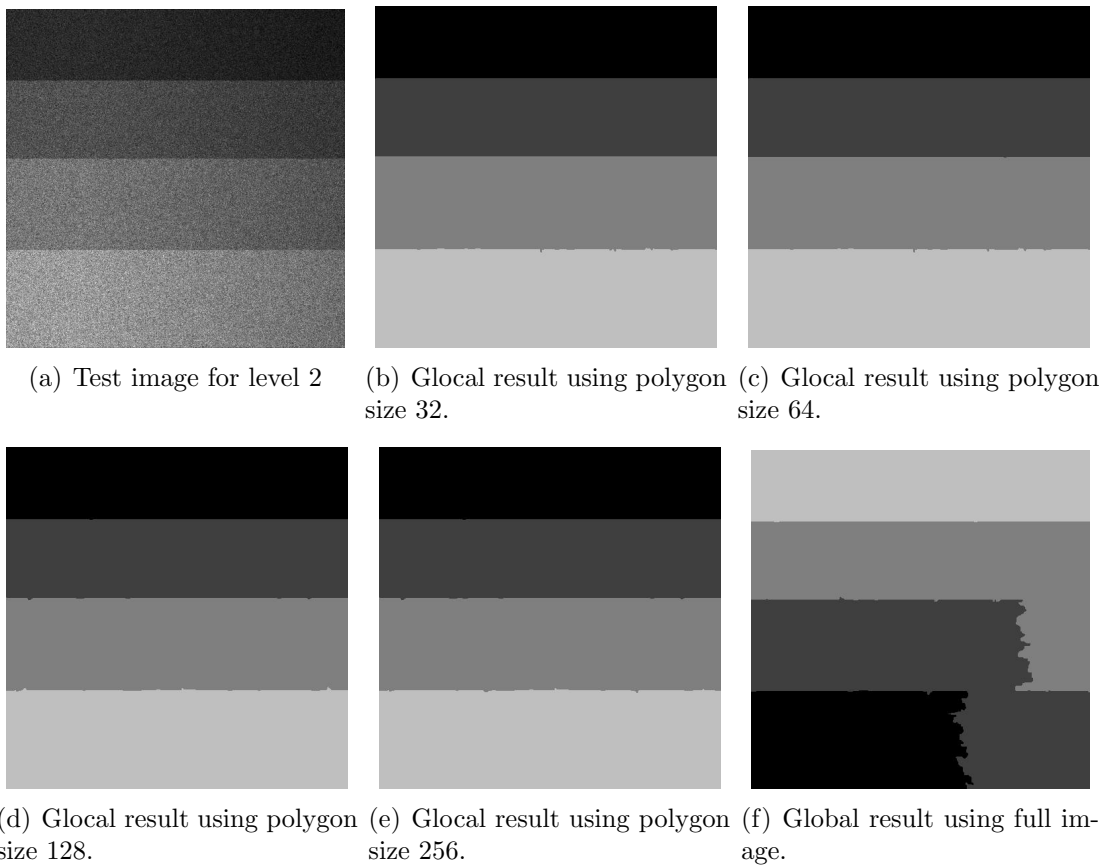


Figure 4.6: Results for four band grey image for illumination level 2.

Although the objective accuracy is quite high, the algorithm fails based on the pass-fail criterion after illumination level 2. Another observation which could be made from the

results is that the brighter strips are misclassified at a much lower illumination gradient. The algorithm can tolerate higher intensity variations for the darker strips irrespective of their width. As the illumination level increases, smaller polygon sizes are seen to perform better as shown in Figure 4.7. A polygon size of 32 yields the best results.

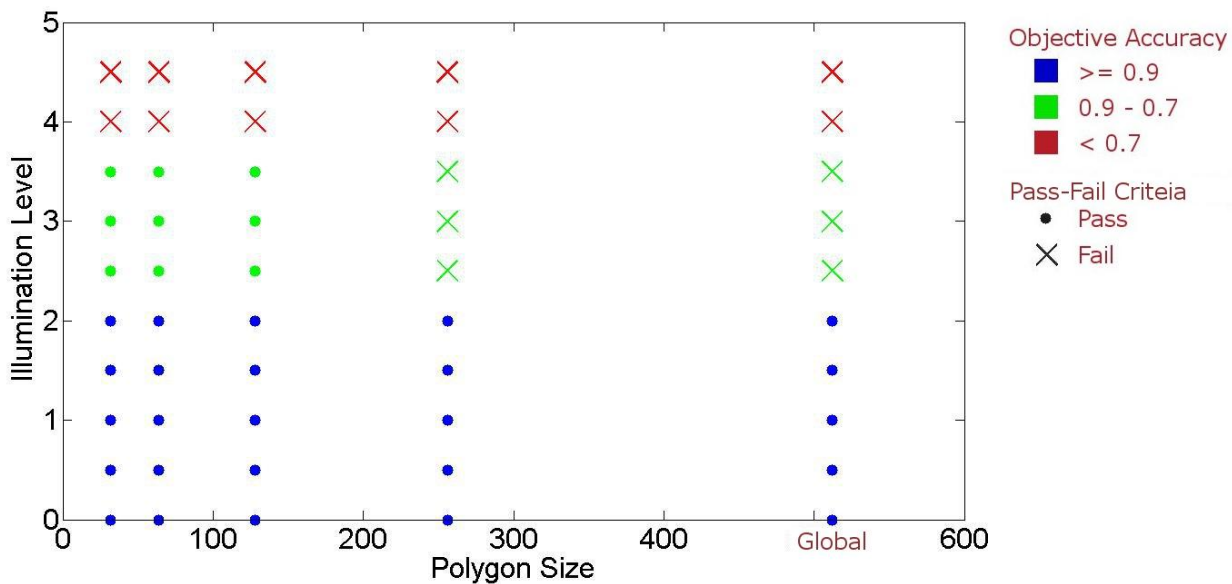


Figure 4.7: Accuracy plot for four band grayscale image (Figure 4.1(a)).

The accuracy for each of the illumination levels and polygon sizes is shown in Table 4.2. The specificity and sensitivity values for both images are shown in Appendix A.1.

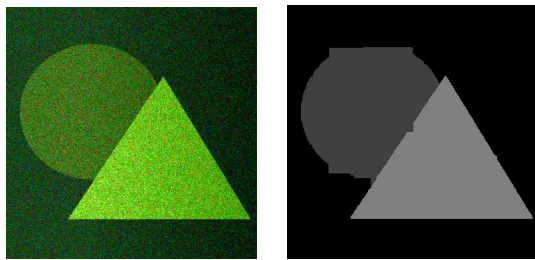
Table 4.2: Accuracy results for four band grey image.

Illumination level	Global Polygon Dimensions (in pixels)				Global
	32x32	64x64	128x128	256x256	
0	0.9998	0.9999	0.9999	0.9999	0.9998
0.5	0.9976	0.9995	0.9995	0.9995	0.9995
1	0.9976	0.9995	0.9994	0.9994	0.9994
1.5	0.9551	0.9992	0.9994	0.9994	0.9994
2	0.9952	0.9990	0.9989	0.9991	0.9990
2.5	0.8392	0.8623	0.8583	0.7191	0.7484
3	0.8372	0.8588	0.8008	0.7035	0.7245
3.5	0.8163	0.8227	0.8011	0.7002	0.7039
4	0.6317	0.6986	0.6906	0.6041	0.6250
4.5	0.6264	0.6633	0.6612	0.6248	0.6062

4.2.2 Colour Image

Similar to the grayscale triangle image, the colour image was also tested until illumination level 4. The classification was observed to break for all polygon sizes above level 3 although the objective metric gave an accuracy above 0.7. The size of the polygons was increased by multiples of two from 16 to 256 since the size of the image is 378x380.

As with the grayscale image, the classification was also affected by the position of the polygons. The blocky artefacts were more prominent in the colour image due to lower contrast. The result for polygon size 64 and illumination level 2, shown in Figure 4.8, illustrates this effect. These artefacts can be avoided by using a shifted grid and more discussion on this issue has been presented in Chapter 7.



(a) Test image for illumination level 2. (b) Glocal result using polygon size 64.

Figure 4.8: Triangle colour image and result for polygon size 64 at illumination level 2.

For illumination level 3, polygon sizes 64 and 128 can identify the triangle because the smaller polygons formed within the triangle when segmented individually are not influenced by the low contrast between the circle and the triangle. However, when IRGS is applied on the entire image, this low edge strength causes the circle and triangle regions to merge as shown in Figure 4.9. The objective accuracies and outcome of the pass-fail measure for all results are plotted in Figure 4.10 and listed in Table 4.3. Appendix A.2 contains the specificity and sensitivity values for the triangle colour image.



(a) Test image for illumination level 3. (b) Glocal result using polygon size 64. (c) Global result for full image.

Figure 4.9: Results for triangle colour image at illumination level 3.

Table 4.3: Accuracy results for triangle colour image.

Illumination level	Glocal Polygon Dimensions (in pixels)				Global
	32x32	64x64	128x128	256x256	
0	0.9992	0.9979	0.9984	0.9979	0.9986
0.5	0.9982	0.9959	0.9964	0.9959	0.9986
1	0.9982	0.9961	0.9958	0.9975	0.9986
1.5	0.9975	0.9940	0.9943	0.9958	0.9984
2	0.9972	0.9955	0.9951	0.9957	0.9980
2.5	0.9975	0.9954	0.9943	0.9955	0.9974
3	0.6990	0.8241	0.8022	0.8115	0.6830
3.5	0.6852	0.7007	0.6916	0.6998	0.6872
4	0.6822	0.6925	0.6905	0.6989	0.6847

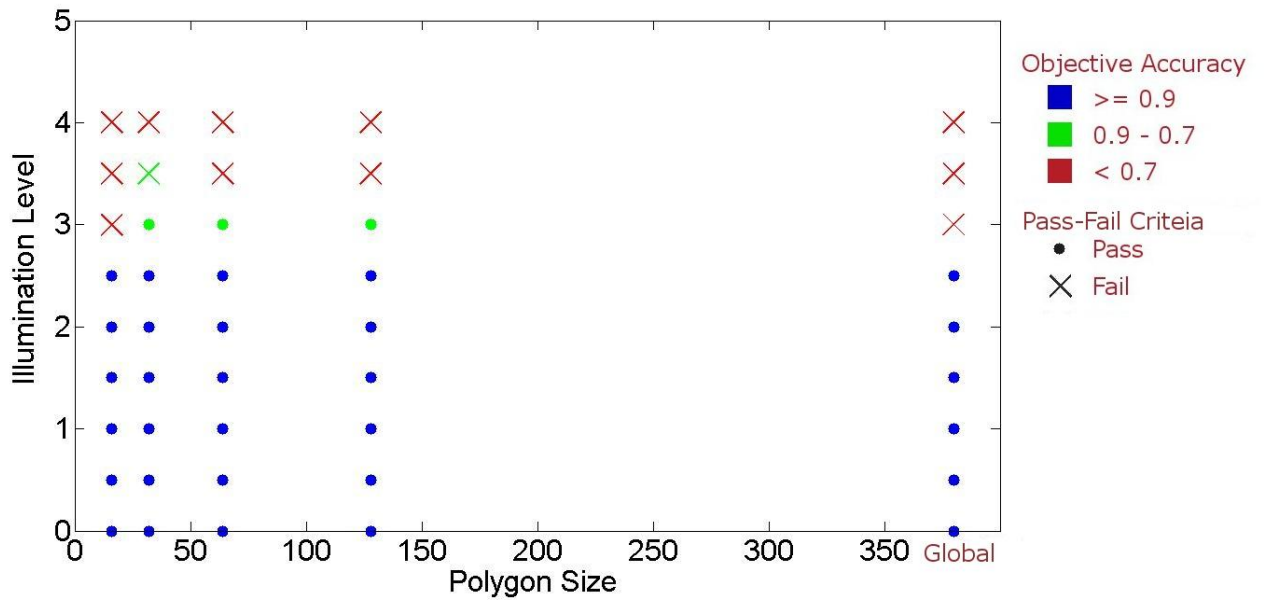


Figure 4.10: Accuracy plot for triangle colour image.

Chapter 5

Testing and Results for Texture Images

5.1 Data

Similar to the four band grey scale image in the previous section, a texture image was generated as shown in Figure 5.1. The width of the four bands from top to bottom was set to 108, 118, 138 and 148 respectively. Four periodic textures were chosen. Since the focus of this research is to identify the sensitivity of the algorithm to illumination variation, these textures were chosen such that they could be distinguished very easily. The illumination level was varied from 1 to 9 with increments of 1 level which is equivalent to 16 grey levels. The size of the image was set to 512x512 pixels. Polygon sizes from 32 to 512 were chosen. Gabor filters were used to extract features for the classification [14]. A total of 24 feature bands were calculated by varying the rotation angle in six directions and the center frequency of the Gaussian envelope over four octaves.

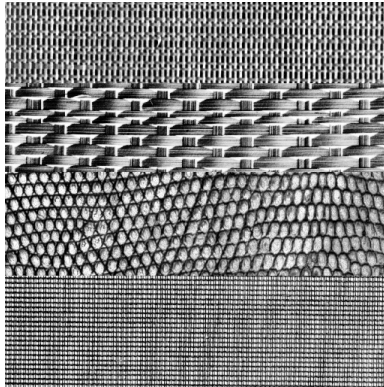


Figure 5.1: Texture test image (512x512).

5.2 Tests and Results

The global result starts failing from illumination level 6. The larger polygon sizes such as 128 and 256 also do not obtain good results for this illumination level. However, polygon sizes 32 and 64 perform much better and can classify the image accurately as shown in Figures 5.2 and 5.3. The accuracy results for different polygon sizes and illumination levels for the glocal approach are shown in Table 5.1. Appendix A.3 contains the specificity and sensitivity values for the various classification tests with the texture image.

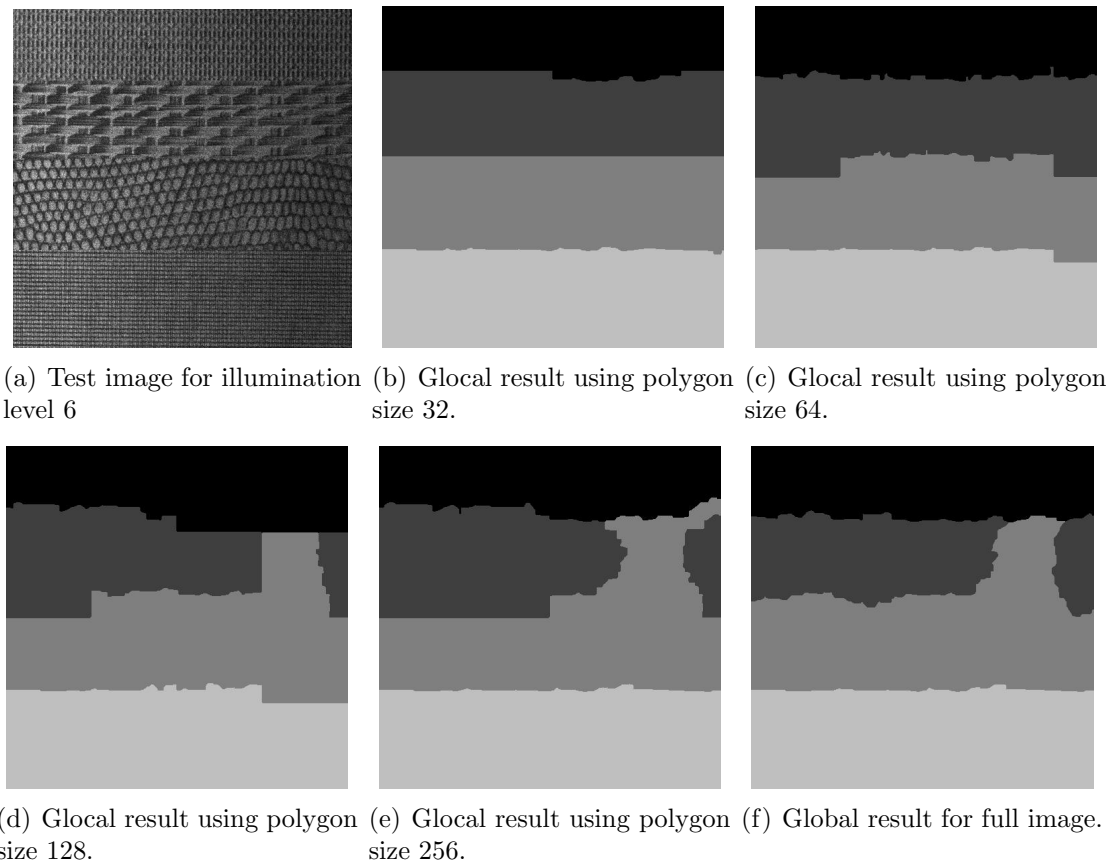


Figure 5.2: Test results for texture image at illumination level 6.

Table 5.1: Accuracy results for texture image.

Illumination level	Glocal Polygon Dimensions (in pixels)				Global
	32x32	64x64	128x128	256x256	
0	0.9964	0.9937	0.9899	0.9871	0.9937
1	0.9944	0.9925	0.9699	0.9771	0.9917
2	0.9916	0.9925	0.9675	0.9720	0.9916
3	0.9902	0.9917	0.9653	0.9721	0.9916
4	0.9905	0.9911	0.9649	0.9811	0.9912
5	0.9911	0.9918	0.9566	0.9746	0.9913
6	0.9697	0.9521	0.8860	0.8926	0.9687
7	0.8961	0.8768	0.7830	0.8957	0.6940
8	0.8017	0.7901	0.7759	0.8493	0.6958
9	0.6818	0.6917	0.6866	0.6657	0.6617

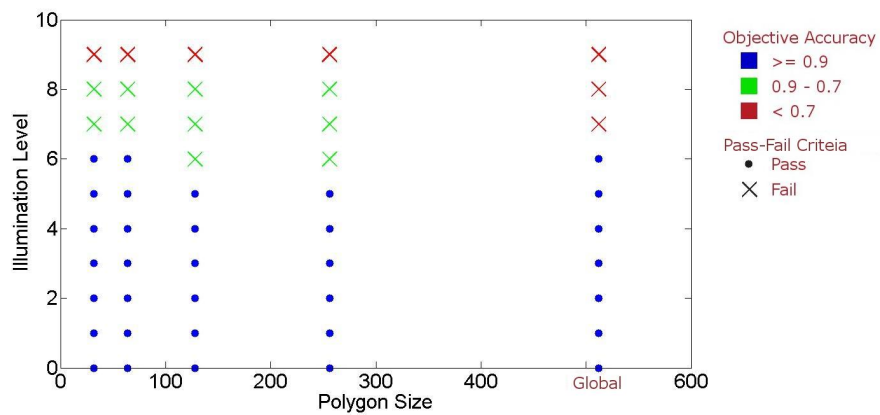


Figure 5.3: Texture image accuracy plot.

For illumination level 7, the global result could not distinguish between the first and the fourth band. It identifies them as belonging to the same class because both the textures are very detailed. Similarly, the second and the third bands are merged because both textures are very repetitive patterns. Figure 5.4 shows that the Glocal approach obtains a better result for polygon size 32 and 128 and yields a higher objective classification accuracy.

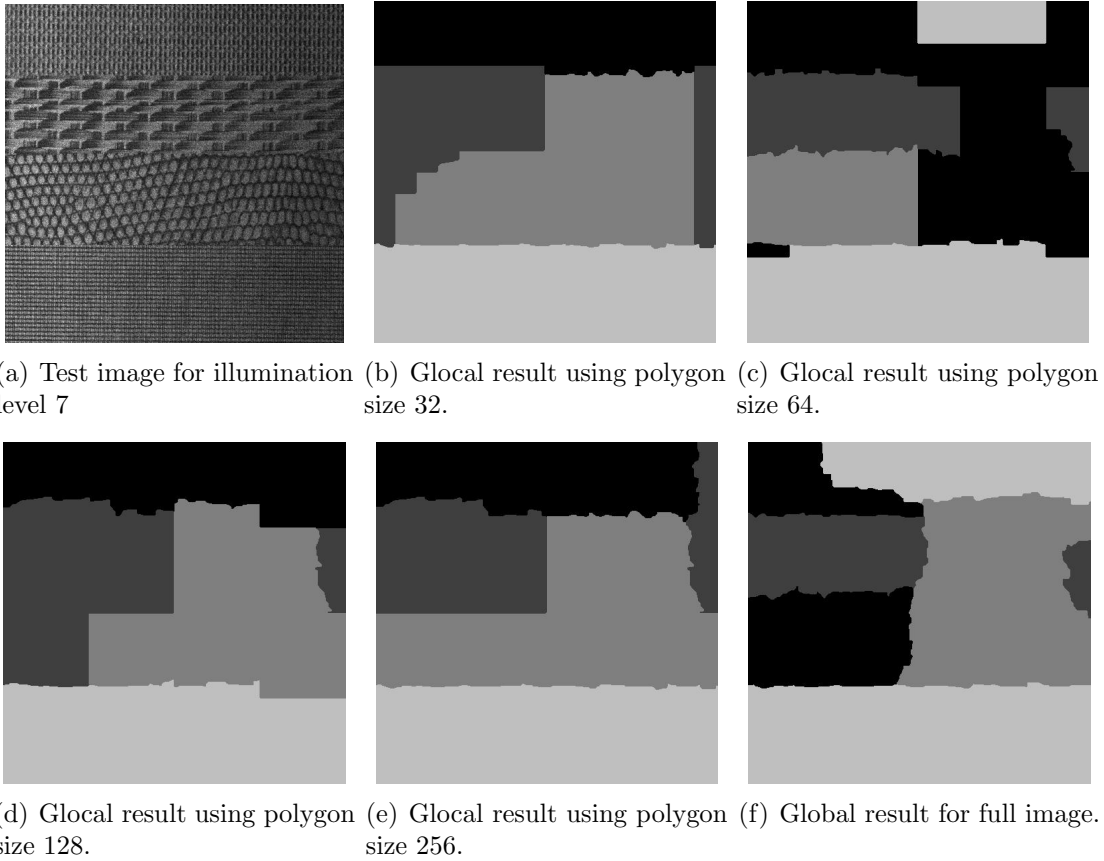


Figure 5.4: Test results for texture image at illumination level 7.

The texture image classification is also observed to be independent of the band heights. The classification is instead influenced by the similarity between the various textures. The algorithm is observed to work for much larger illumination gradients with feature extraction. The various features which are extracted gives the algorithm more information to work with than just grey level. Similarly, the algorithm can classify the colour triangle image for one illumination level more than the grayscale triangle image as it has three different bands and employs IRGS for the various steps involved in the Glocal approach.

Chapter 6

Testing and Results for SAR Images

6.1 Data

SAR images were obtained from the Canadian Ice Service (CIS) and McDonald Dettwiler and Associates (MDA). All the images that were tested are RADARSAT-II dual-band images. Each image has an HH and HV band. The image data available was not suitable to test the Glocal approach because of variations and anomalies in the SAR images caused by factors other than the incidence angle effect. For concept testing, one of the SAR image was cropped to remove the effects caused by these factors. Since there are no other external effects in the sub-image shown in Figure 6.1, it can be considered a fair test.

Two full scene SAR images, shown in Figure 6.2 and Figure 6.3, were tested as well. Both the HH and HV bands of each image are shown.

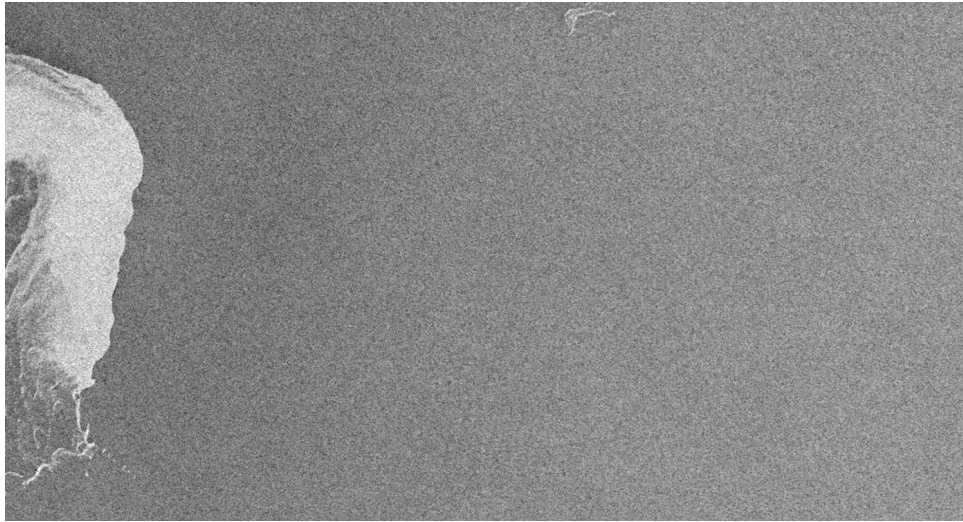


Figure 6.1: Cropped SAR test image for the HH band (1494x805).



(a) HH band

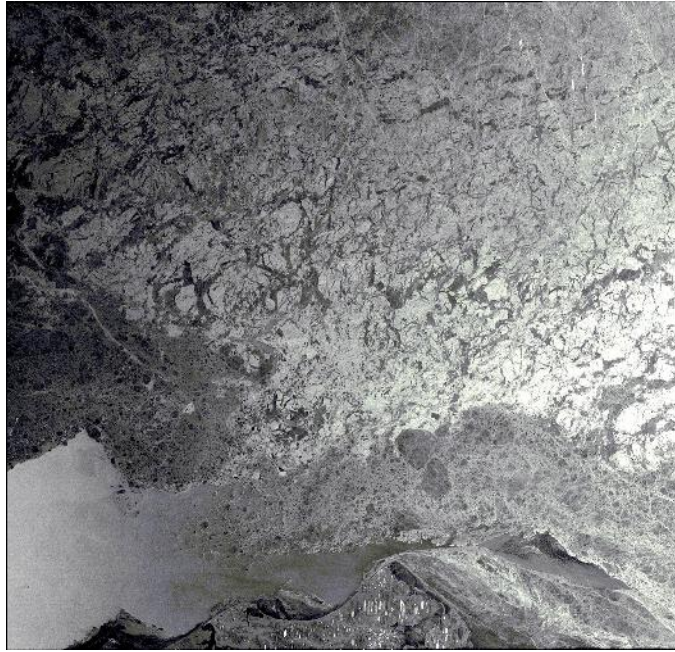


(b) HV band

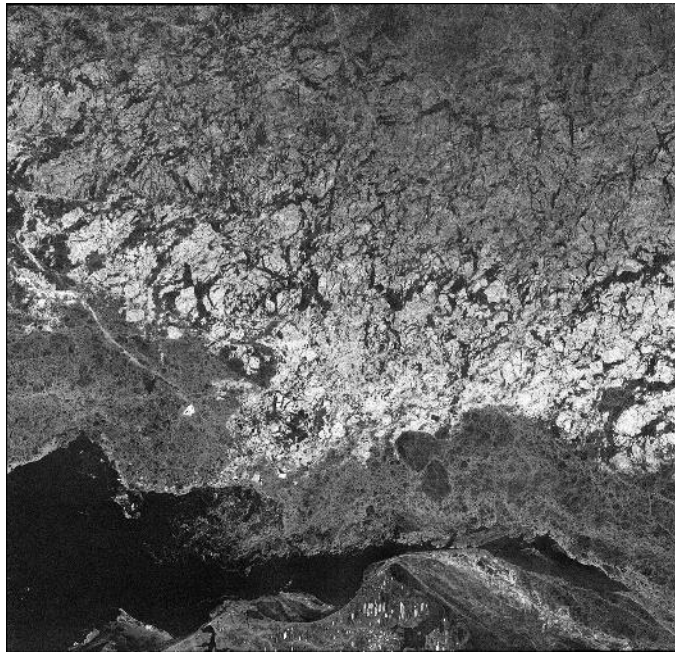
Figure 6.2: RADARSAT-2 Image taken on April 01, 2010 (10487x9620 pixels).

The image shown in Figure 6.2(a) demonstrates a very strong incidence angle effect in its HH band. There are also spatial intensity variations in the image, such as the dark patch in the top right, caused by other environmental factors. The image in Figure 6.2(b) shows the HV band which also has a dominant banding effect. The illumination does not vary gradually in these images, as it would be expected to, if the images were free of other artefacts.

The second SAR image, illustrated in Figure 6.3, has been filtered, at source by MDA, with the Lee sigma filter [41] to remove the banding effect in the HV band shown in Figure 6.3(b). The HH band, shown in Figure 6.3(a), has also been filtered.



(a) HH band



(b) HV band

Figure 6.3: RADARSAT-2 Image (10557x10114 pixels).

This filtering method however introduces other artefacts in the image and distorts the texture of the SAR data and blurs the boundaries between various classes. A zoomed in area of the HH band, shown in Figure 6.4, demonstrates this effect. Improving the raw data is an ongoing effort at MDA. However, better data was not available for this research. Due to limited availability of clean SAR images extensive testing could not be performed.

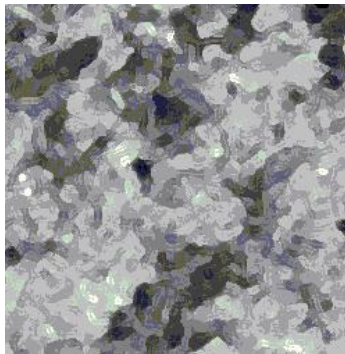
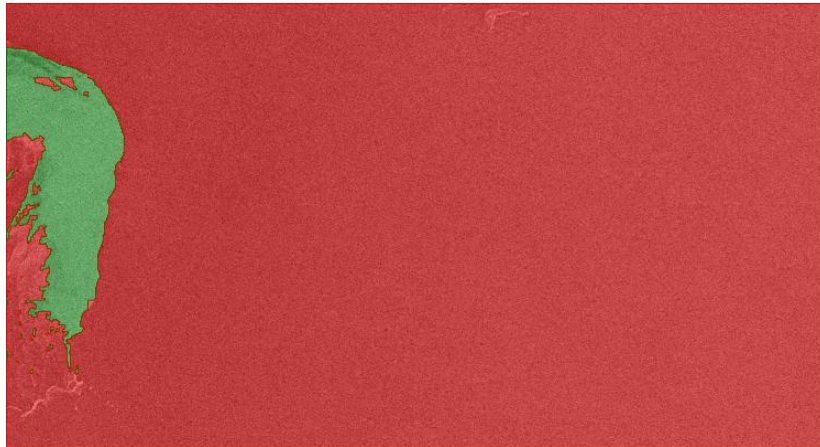


Figure 6.4: Wormy appearance of the HH and HV bands (scale 1:1).

6.2 Tests and Results

The results for the cropped image are demonstrated both with the Glocal approach and with IRGS applied on the full scene in Figure 6.5(a) and Figure 6.5(b) respectively. IRGS when applied on the whole image breaks the open water into two classes. However, the Glocal approach correctly segments the full scene and preserves the wispy details of the sea ice seen in the image. The polygon size chosen for the Glocal approach was 150x100 which is roughly one-tenth of the dimensions of the image.

To illustrate the various steps in the Glocal approach, the different stages in this process are shown for the cropped SAR image in Figure 6.6. A polygon grid is formed based on the chosen polygon size. This is followed by setting up the global label list and initializing the labels for each polygon. In this case, the global label list contains two classes and each polygon is assigned all the labels in the global list automatically. Each polygon is then segmented individually with IRGS. The final result is obtained by gluing the intermediate result of all polygons together with IRGS.

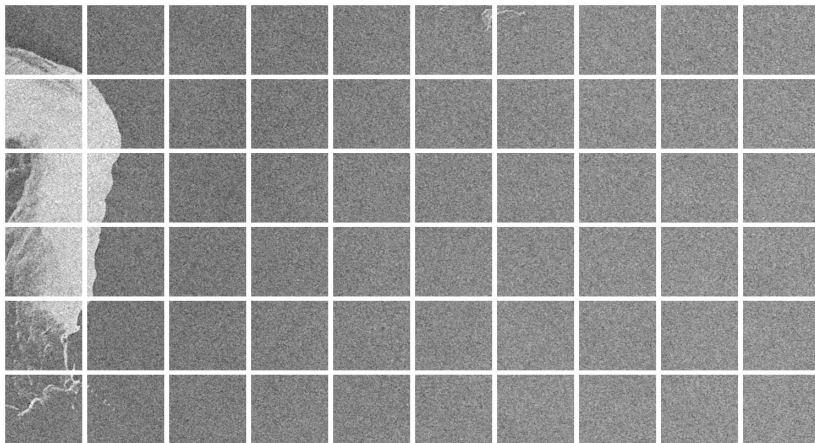


(a) Glocal result for polygon size 128.

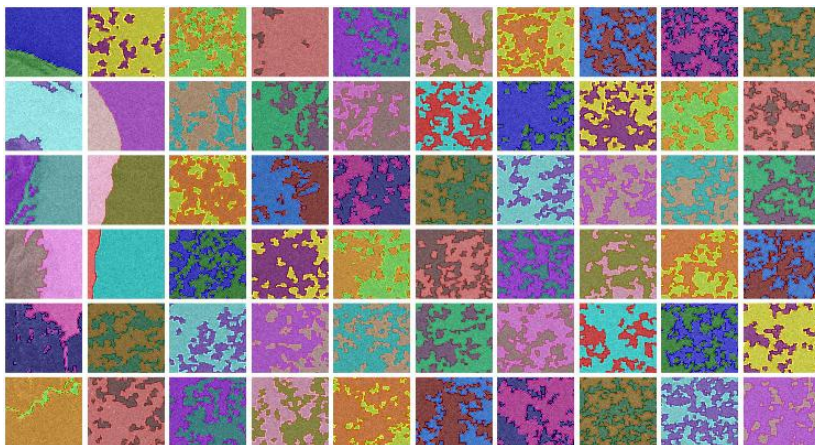


(b) Global result.

Figure 6.5: Full scene classification for the cropped image shown in Figure 6.1.



(a) Polygon Grid formed using a polygon size of 128x128

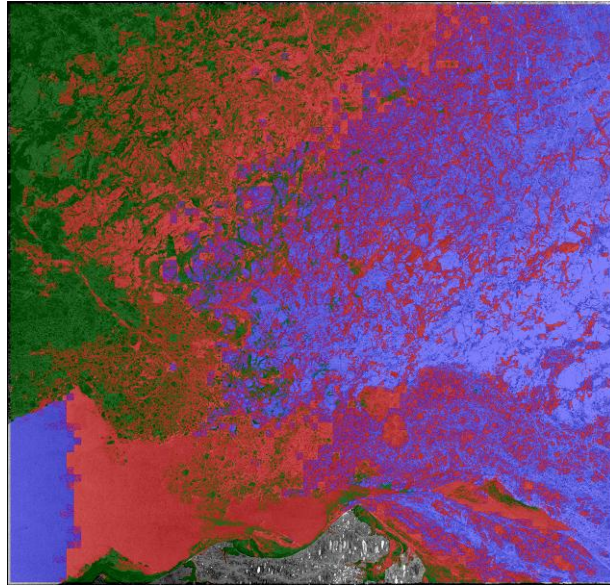


(b) Result of step 3 as explained on page 18. Here, each polygon is classified independently using IRGS.

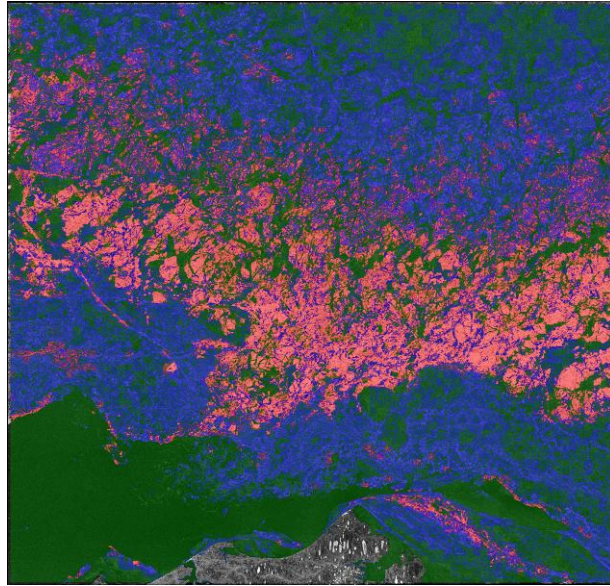
Figure 6.6: Different stages of the Glocal approach.

The dimensions of both the SAR test images is approximately 10000x10000 pixels. Results for the SAR image in Figure 6.3 are shown in Figure 6.7 and Figure 6.8. The global label list was initialized to three labels. Since the image contains sea ice of two different types, three classes were chosen to initialize the full scene labels. Each polygon in the image was also assigned all three classes.

Two different polygon sizes were tested. The results for the 128x128 polygons are shown in Figure 6.7. The result for the HV band is promising. However, the HH result misclassifies both ice and open water. The result for the multi-band image, that is both HH and HV combined, does not break the open water into two segments but it fails to identify the sea ice. The result reintroduces the issues noticed in the HH band.



(a) HH

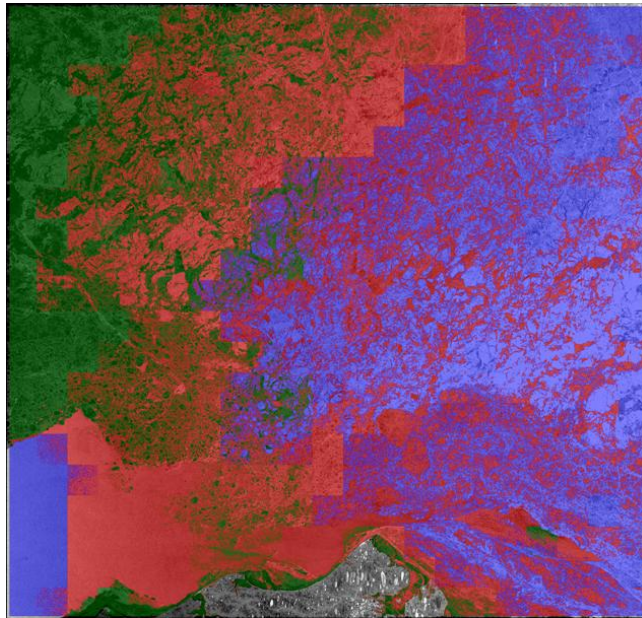


(b) HV

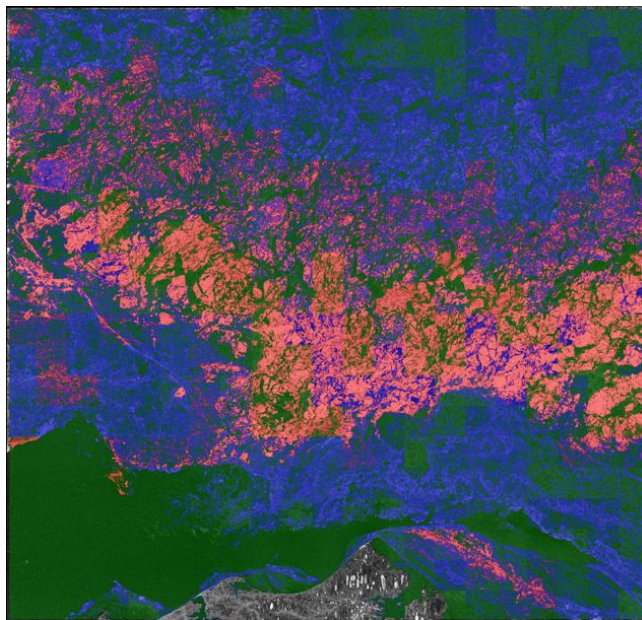
Figure 6.7: Glocal results for HH and HV bands for polygon size 128 when the Glocal approach is applied to Figure 6.3. The HH band (a) has a strong illumination effect due to which the Glocal approach fails and breaks down the open water into two classes. The HV band (b) gives reasonable results.



Figure 6.8: HH,HV Glocal result for Figure 6.3 for polygon size 128. The strong illumination in HH throws off the algorithm. Blocky artefacts are introduced.



(a) HH



(b) HV

Figure 6.9: Result of the Glocal method for polygon size 512 applied to HH and HV bands shown in Figure 6.3. The Glocal method fails for HH (a). The HV band (b) gives a reasonable result but shows some blocky artefacts.

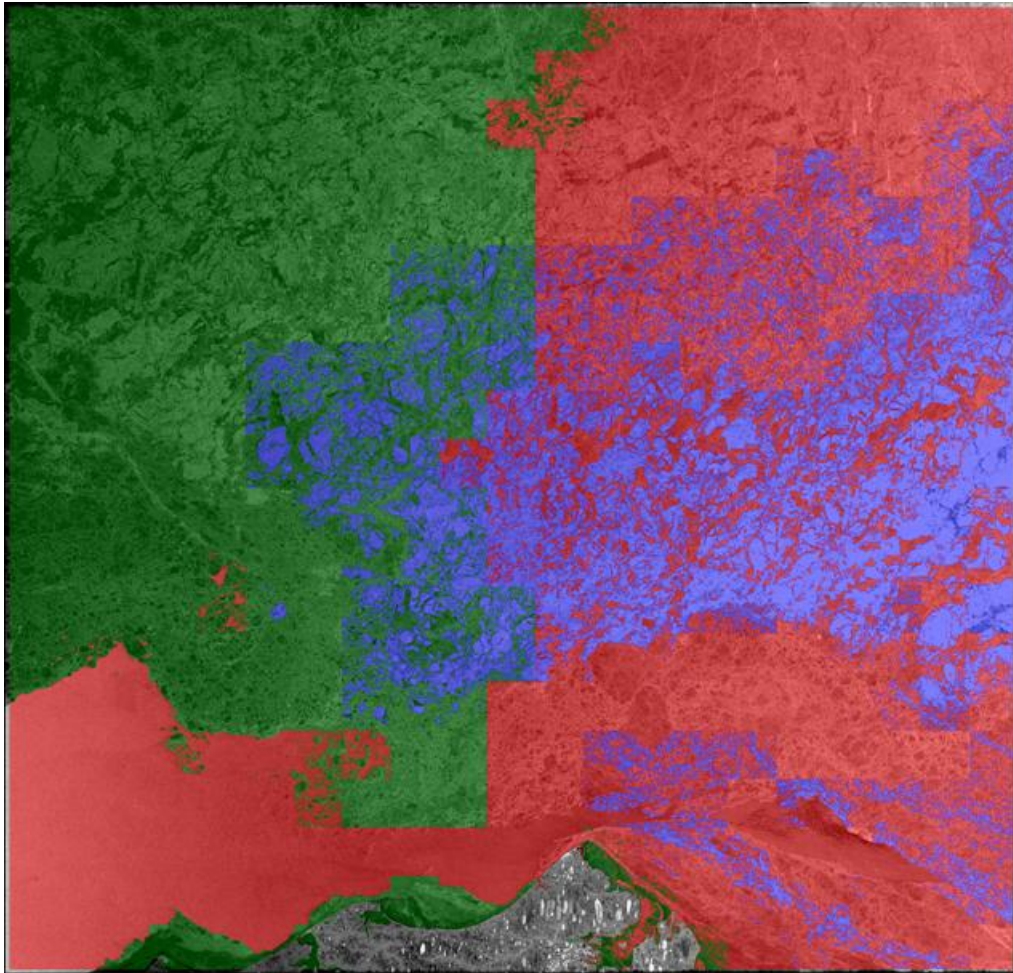


Figure 6.10: Result of the Glocal approach applied to the dual band SAR image in Figure 6.3 for polygon size 512. The result is blocky and although the water is not misclassified, the issues from HH band are included.

For a polygon size of 512x512, blocky artefacts are introduced because IRGS fails to merge across the polygon boundaries in these regions. This can be attributed to the underlying data which was modified due to preprocessing. To summarize, smaller polygon sizes such as 128x128 obtain good results. Since only the HV band yielded reasonable results, the IRGS result for the HV band alone is shown in Figure 6.11. The algorithm fails to classify the full scene.

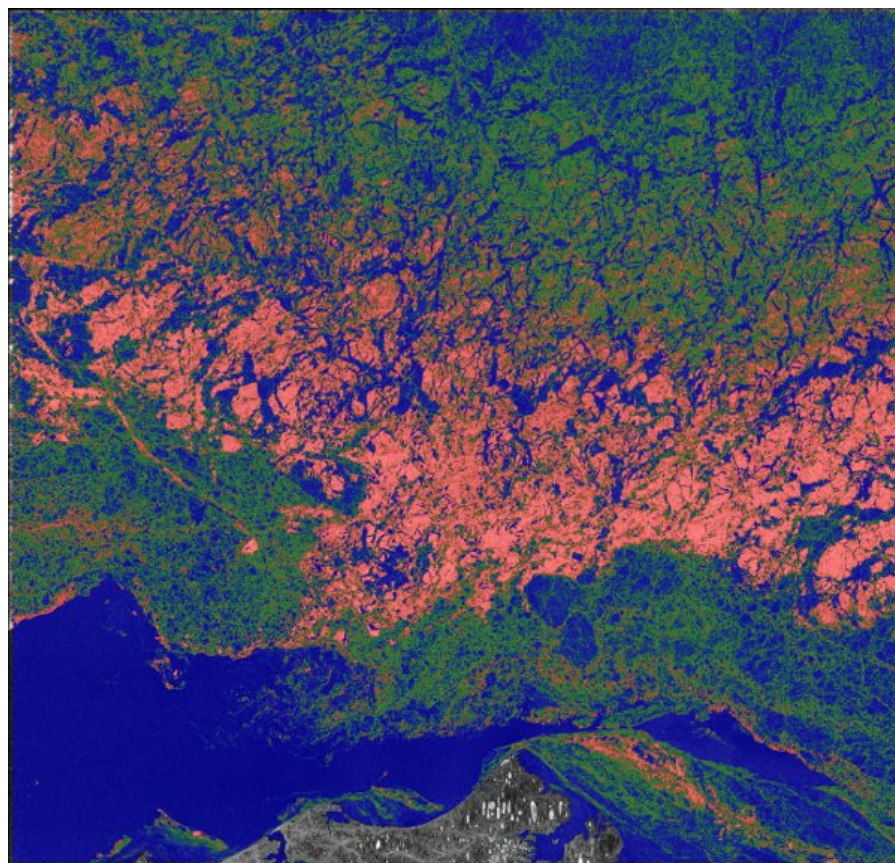
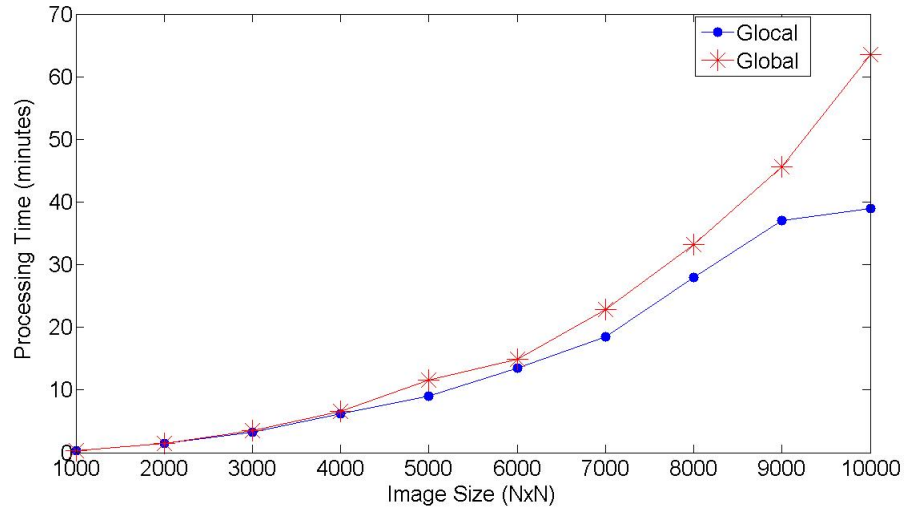
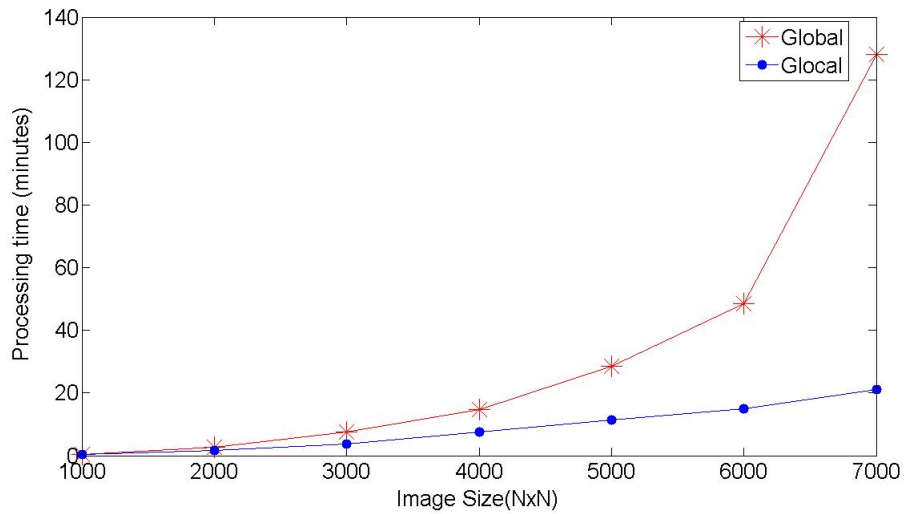


Figure 6.11: Global result for HV band for Figure 6.3. The global approach misclassifies ice in the upper half of the image.

Figures 6.12(a) and 6.12(b) show the relationship between processing time and image dimensions for the global and Glocal results with the HV band and dual band image respectively. The tests were run on a 16 GB, 3.10GHz machine. The processing time for single band increases linearly but for dual band it increases exponentially for the global method. The Glocal approach is computationally cheaper and runs in the order of minutes, while the processing time for the global technique is in the order of hours, for larger images with more than one bands. This is because when IRGS is applied to the full scene the whole image is broken down into small regions, which are then merged iteratively. However, for the Glocal approach, IRGS is applied on each polygon first. So, the number of regions which need to be merged iteratively is much smaller. When IRGS is applied on the entire scene again, the regions which need to be merged are big and hence very few.



(a) Processing time for HV band alone.

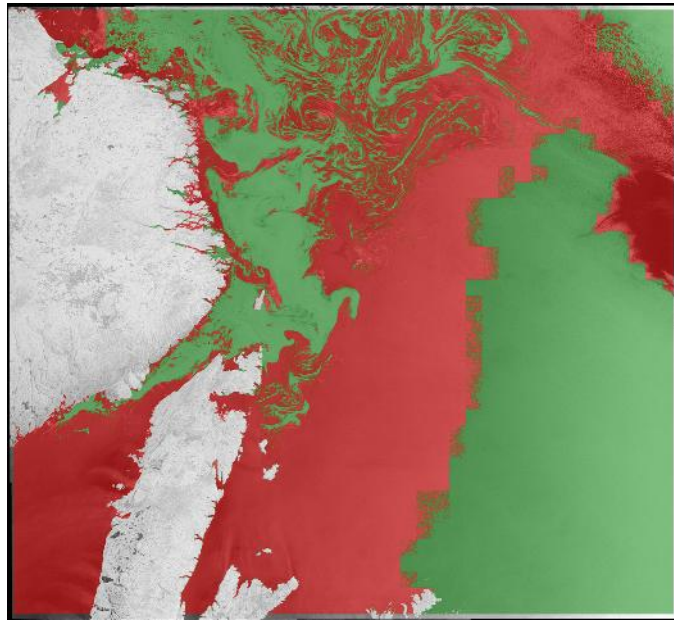


(b) Processing time for dual band image.

Figure 6.12: Relationship between processing time and image size for Global and Glocal methods.

Since, the global method fails for the cropped image and the Lee filtered SAR image, the rest of the images were not tested for IRGS full scene segmentation. The results of Glocal approach for the SAR image, shown in Figure 6.2, are demonstrated in Figure 6.13 for both the bands. The global label list was initialized to two classes (ice and open water). Each polygon in the image was also assigned both the labels.

The tests for Figure 6.2 are conducted for only the 128x128 polygon size, as shown in Figure 6.13, because the bigger polygon sizes were observed to give blocky and less accurate results for other images. The Glocal method fails to classify the image for both the HH and HV bands. The algorithm fails mainly because of two reasons: the nature of the image data and the parameters for the gluing step. For the HH band, the illumination gradient is very strong. While the Glocal approach can handle moderate illumination changes, it fails under strong illumination conditions because it still employs the Gaussian statistics in the gluing stage. Also, the image contains artefacts caused by other environmental factors. Even though the open water in the bottom left and top left of the image is spatially isolated from the rest of the open water, the algorithm could merge the regions well. Setting the parameters for the gluing step optimally is also essential for a successful classification. Experiments were conducted by starting the gluing process with a different set of parameters which would place a higher weight on the edge strength criterion. However, there was no significant improvement in the results as discussed in Section 7.2.



(a) HH



(b) HV

Figure 6.13: SAR Test results applied to Figure 6.2 for polygon size 128. The Glocal approach fails because of the strong illumination in HH and banding effect in HV. The results show that the open water is misclassified in both the bands.

The IRGS parameters used for the gluing process were also investigated. Since each of the polygons was segmented after the first step of the Glocal approach, the second step should focus more on merging the regions based on the edge strength between them. Due to variability in the image, the algorithm needs to glue the larger regions by considering the edge strength rather than the Gaussian statistics.

For all the tests, IRGS was run with its default settings, and hence the Gaussian statistics had a greater impact in the initial stages of the merging in stage two and the edge strength was given a higher priority later on in the iterative merging process. This could have led the algorithm to fail for the HH band.

For concept testing, we tried starting the IRGS algorithm from iterations 50 and 80 for the iterative merging process. The total number of iterations were user-defined but it has been recommended to be set to 100 [2]. Since the iterations were started mid-way, the parameters would be adapted such that the edge strength criterion had a greater impact. Figures 6.14(a) and 6.14(b) show the result of the Glocal approach when the iterations were started from 50 and 80 respectively. There is no improvement as seen in the results.



(a) Result for iterations starting from 50



(b) Result for iterations starting from 80

Figure 6.14: Result obtained by changing gluing parameters.

Chapter 7

Conclusion and Future Work Recommendations

7.1 Summary

A technique was developed that helped to improve classification accuracy for images under illumination changes. The IRGS algorithm was observed to improve the classification accuracy of images substantially as compared to other algorithms [3]. However, it was unable to deal with gradual changes in illumination across the scene, where such illumination modifies class statistics. A novel two step hierarchical approach, called the Glocal method, was investigated and the performance of the algorithm was analysed for different parameters. The algorithm starts by partitioning the image in a rectangular grid based on a user selected polygon size. Each polygon is then segmented using IRGS. The final classification is obtained by gluing all the locally segmented regions using IRGS on a global scale.

This method was shown to be efficient for both general classification and SAR sea ice and open water discrimination. The Glocal method would help in automating the process of estimating ice and water concentration in polygons and would give an initial estimate for the sea ice analyst.

The Glocal method was tested with a variety of images. Experiments were performed on three SAR images and four other simulated images. The test dataset for the simulated images consists of a colour image (Figure 4.2), two grayscale images (Figure 4.1) and one Brodatz texture image (Figure 5.1). The results of the Glocal approach on these

images showed that choosing a polygon size which is one-tenth the size of the image gave a reasonably accurate result. Smaller polygon sizes (32 and 64) performed better than larger polygons. The classification was observed to be dependent on the positioning of the polygons, and hence the contents of the image, which introduced blocky artefacts in the resulting classification. The results for the four band grey image, shown in Figure 4.1(a), indicate that the algorithm has lower sensitivity to illumination variation for a lower mean grey level.

The Glocal approach performs significantly better than IRGS for classifying images with illumination variation and SAR speckle noise. Open water and new ice appear dark in the HV band of SAR images. Both these surfaces are very smooth compared to other types of sea ice. New ice does not pose a navigational hazard for ships. Hence, it is sufficient to use only the HV band to distinguish between ice and open water. The Glocal method can segment the HV band successfully if there are no banding effects in the image. However, it fails to classify the HH band in SAR images. The algorithm cannot tolerate the strong illumination variation and other anomalies in the HH band.

The questions posed in Section 2.4 can now be answered.

1. How can we overcome spatial illumination variation in images, for the purpose of image classification, regardless of the illumination model?

The Glocal approach was observed to be robust to spatial illumination variation to a greater extent than using the standard global approach. Although, the tests were only performed for SAR incidence angle effect illumination changes, the algorithm did not model the illumination variation and was designed to overcome any gradual intensity variation within the same class.

The Glocal approach could successfully delineate sea ice from open water based on the denoised HV band alone. The HV band had sufficient information for discriminating the two classes. However, the algorithm failed to classify the HH band accurately.

2. Can this method be applied to process large images like SAR sea ice images efficiently?

The bottleneck with IRGS and the Glocal approach was the amount of memory that the algorithm needs, due to the large size of the images. IRGS can take several days to process a full scene image on a computer with 12GB RAM. On the other hand, the Glocal method takes approximately an hour to complete the classification for a full

scene SAR image on the same computer. Since the SAR images were processed on a daily basis, a runtime of multiple days to process a single image is impractical, and not very useful to guide the analysts. However, using the Glocal technique would be reasonable as the images could be processed overnight.

The Glocal method was computationally less expensive as it partitions the image into smaller region and runs IRGS on each region individually. The computational time for IRGS grows exponentially with the size of the region. Hence, by using a divide and conquer approach, the Glocal algorithm could produce results in a reasonable amount of time.

3. What would be the best set of parameters for this approach?

The sensitivity of the algorithm for different polygon sizes was investigated. Several test images were generated by varying the illumination gradient in gradual steps. A constant amount of speckle noise representative of SAR noise was added to all simulated images.

It was observed that for general classification, smaller polygon sizes around one-tenth (32 or 64 pixels) the size of the image produced reasonable results. For larger images like SAR, the polygon size of 128 yielded reasonable results. Larger polygon sizes produced results with blocky artefacts.

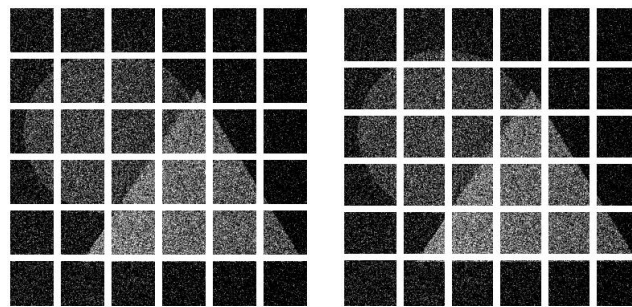
The positioning of the polygon and hence the image contents were observed to affect the classification results. This issue is discussed in more detail in Section 7.2. In summary, for images with dimensions less than 1000x1000 pixels, a polygon size of 64x64 gave the best results. For large SAR images, a polygon size of 128x128 produced a reasonable classification for the denoised HV band. If the polygon size was chosen to be too large or too small the classification failed and introduced artefacts in the resulting image.

7.2 Future Work Recommendations

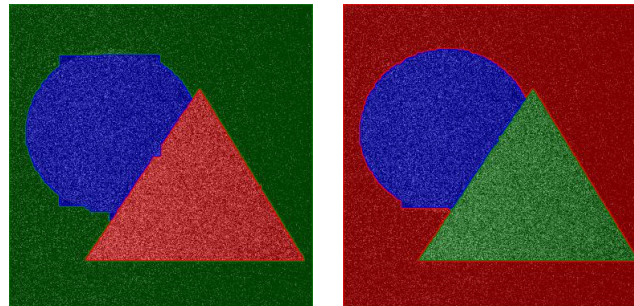
The Glocal method proposed in this thesis can be improved in several ways. Some ideas that could be investigated in the future are listed below.

1. The classification results depend on the placement of the polygons based on the generated polygon grid. Blocky artefacts were generated if the positioning of the

polygons was such that only a small segment of one of the classes was present in the polygon. If the grid was moved by a small offset, the classification for the corresponding polygon did not show any artefacts. This is illustrated in Figure 7.1(b). The original grid and the corresponding shifted grid is shown in Figures 7.1(a) and 7.1(b) respectively. The shifted grid was generated by introducing an offset in the original grid, along the row and the column directions, by a few pixels. As illustrated in Figure 7.1(d), the offset improved the results for a few of the individual polygons and reduced the blocky artefacts.



(a) Original polygon grid (b) Shifted grid



(c) Result with original grid (d) Result with shifted grid

Figure 7.1: Removing blocky artefacts by moving the grid.

Future work can focus on only extracting the result inside a polygon which is common to the original grid and the shifted grid as this result is less likely to be affected by boundary conditions. Generating a rotated grid and investigating its effect on the results is another idea which could be explored.

2. A promising area for future work is to investigate whether the number of levels of hierarchy would affect the final classification result. More stages can be added to the

hierarchical approach. Instead of merging all the individual polygon results together with IRGS in the second step, the polygons could only be glued with their immediate neighbours. Each hierarchical stage would consist of first merging the polygon with its neighbour (right or left) in the horizontal direction and then with its neighbour (top or bottom) in the vertical direction. The order of the merging can be swapped to analyse the performance of the algorithm. Building the result in such a hierarchical manner would make the algorithm more robust to illumination variation.

3. Although the divide and conquer approach helps in reducing the processing time of the IRGS algorithm significantly, there is potential for further improvement. Since each of the polygons is segmented individually in the first step, they can be processed in a parallel fashion instead of serially processing them. Parallel processing can be accomplished by using multi-threading and multiple cores. The speed of the algorithm can be further improved by using Graphical Processing Units (GPUs). Employing such techniques would improve the processing time of the algorithm significantly and would make it more usable for analysts at CIS.
4. The IRGS parameters used for the gluing process were not investigated thoroughly in this thesis. In Section 6.2, the impact of various number of iterations was studied. Lower number of iterations correspond to using a higher weight for the edge strength while gluing, whereas a higher number of iterations implies using the edge strength initially and then relying on the Gaussian statistics to merge the regions. There was no significant improvement observed in the results. A future area of research would be to explore how the parameters vary throughout the iterative process. Using edge strength alone for the gluing stage can be further investigated. Texture features can also be used along with the edge strength to overcome the dependency of the algorithm on the grey level of the regions.

APPENDICES

Appendix A

Sensitivity and Specificity Results for Classification Tests

A.1 Performance Measures for Grayscale Images

Table A.1: Sensitivity results for triangle grey image.

Illumination level	Glocal Polygon Dimensions (in pixels)				Global
	32x32	64x64	128x128	256x256	
0	0.9995	0.9996	0.9996	0.9995	0.9995
0.5	0.9992	0.9958	0.9995	0.9995	0.9994
1	0.9991	0.9957	0.9994	0.9993	0.9994
1.5	0.5774	0.9954	0.9990	0.9990	0.5585
2	0.5628	0.9954	0.9992	0.9921	0.5691
2.5	0.5639	0.9954	0.9991	0.9991	0.5593
3	0.5427	0.5488	0.5385	0.5809	0.5447
3.5	0.5412	0.5424	0.5384	0.5776	0.5404
4	0.5402	0.5416	0.5384	0.5750	0.5401

Table A.2: Specificity results for triangle grey image.

Illumination level	Glocal Polygon Dimensions (in pixels)				Global
	32x32	64x64	128x128	256x256	
0	0.9998	0.9979	0.9998	0.9997	0.9998
0.5	0.9996	0.9979	0.9998	0.9997	0.9998
1	0.9996	0.9979	0.9997	0.9996	0.9997
1.5	0.7814	0.9977	0.9995	0.9995	0.7845
2	0.7737	0.9977	0.9996	0.9960	0.7792
2.5	0.7720	0.9977	0.9996	0.9996	0.7790
3	0.7713	0.7744	0.7693	0.7904	0.7723
3.5	0.7712	0.7742	0.7689	0.7888	0.7716
4	0.7711	0.7743	0.7682	0.7925	0.7702

Table A.3: Sensitivity results for four band grey image.

Illumination level	Glocal Polygon Dimensions (in pixels)				Global
	32x32	64x64	128x128	256x256	
0	0.9997	0.9998	0.9998	0.9999	0.9998
0.5	0.9976	0.9995	0.9995	0.9995	0.9995
1	0.9966	0.9995	0.9994	0.9994	0.9984
1.5	0.9551	0.9992	0.9994	0.9994	0.9994
2	0.9952	0.9990	0.9989	0.9991	0.9990
2.5	0.8092	0.8423	0.8383	0.7091	0.7384
3	0.8072	0.8388	0.8008	0.7035	0.7245
3.5	0.8063	0.8227	0.8011	0.7013	0.7039
4	0.6317	0.6986	0.6906	0.6041	0.6250
4.5	0.6264	0.6633	0.6612	0.6248	0.6062

Table A.4: Specificity results for four band grey image.

Illumination level	Glocal Polygon Dimensions (in pixels)				Global
	32x32	64x64	128x128	256x256	
0.5	0.9850	0.9997	0.9998	0.9998	0.9998
1	0.9992	0.9998	0.9998	0.9998	0.9998
1.5	0.9992	0.9998	0.9998	0.9998	0.9998
2	0.9984	0.9997	0.9997	0.9997	0.9996
2.5	0.8864	0.8808	0.8928	0.8064	0.8095
3	0.8457	0.8529	0.8336	0.7678	0.7515
3.5	0.8439	0.8529	0.8335	0.7680	0.7483
4	0.8388	0.8409	0.8337	0.7680	0.7479
4.5	0.7855	0.7878	0.7871	0.7349	0.6954

A.2 Performance Measures for Colour Images

Table A.5: Sensitivity results for triangle colour image.

Illumination level	Glocal Polygon Dimensions (in pixels)				Global
	32x32	64x64	128x128	256x256	
0	0.9993	0.9979	0.9985	0.9978	0.9998
0.5	0.9973	0.9939	0.9945	0.9938	0.9978
1	0.9973	0.9942	0.9937	0.9962	0.9978
1.5	0.9963	0.9933	0.9927	0.9937	0.9976
2	0.9963	0.9910	0.9915	0.9936	0.9971
2.5	0.9958	0.9901	0.9915	0.9933	0.9972
3	0.6996	0.7487	0.7021	0.7092	0.5245
3.5	0.5278	0.7061	0.5374	0.5692	0.5308
4	0.5232	0.5361	0.5357	0.5633	0.5271

Table A.6: Specificity results for triangle colour image.

Illumination level	Glocal Polygon Dimensions (in pixels)				Global
	32x32	64x64	128x128	256x256	
0	0.9992	0.9979	0.9984	0.9979	0.9996
0.5	0.9982	0.9959	0.9964	0.9975	0.9986
1	0.9982	0.9961	0.9958	0.9959	0.9986
1.5	0.9975	0.9955	0.9951	0.9958	0.9984
2	0.9972	0.9954	0.9943	0.9957	0.9980
2.5	0.9975	0.9940	0.9943	0.9955	0.9981
3	0.6922	0.8241	0.8370	0.7115	0.6830
3.5	0.6852	0.7507	0.6916	0.7128	0.6872
4	0.6822	0.7325	0.6905	0.7089	0.6847

A.3 Performance Measures for Texture Images

Table A.7: Sensitivity results for texture image.

Illumination level	Glocal Polygon Dimensions (in pixels)				Global
	32x32	64x64	128x128	256x256	
0	0.9898	0.9848	0.9498	0.9652	0.9845
1	0.9888	0.9835	0.9398	0.9543	0.9835
2	0.9833	0.9850	0.9350	0.9540	0.9839
3	0.9805	0.9851	0.9298	0.9542	0.9831
4	0.9909	0.9862	0.9306	0.9495	0.9843
5	0.9822	0.9836	0.9132	0.9492	0.9846
6	0.9394	0.9042	0.8720	0.8651	0.9374
7	0.8321	0.7535	0.7660	0.7313	0.6299
8	0.6034	0.6802	0.6520	0.6985	0.5415
9	0.5635	0.5833	0.5732	0.5313	0.5234

Table A.8: Specificity results for texture image.

Illumination level	Glocal Polygon Dimensions (in pixels)				Global
	32x32	64x64	128x128	256x256	
0	0.9972	0.9953	0.9802	0.9852	0.9947
1	0.9963	0.9945	0.9799	0.9848	0.9945
2	0.9944	0.9950	0.9783	0.9813	0.9947
3	0.9935	0.9950	0.9766	0.9814	0.9944
4	0.9970	0.9954	0.9769	0.9794	0.9947
5	0.9940	0.9945	0.9711	0.9781	0.9949
6	0.9798	0.9681	0.9240	0.9384	0.9791
7	0.9440	0.9178	0.8553	0.8771	0.8433
8	0.8678	0.8601	0.8507	0.8995	0.7939
9	0.8545	0.8611	0.8578	0.8440	0.7411

Appendix B

Matlab Code for Simulating SAR Illumination and Noise

```
function [Result] = AddIlluminationGradient(InputImage, SimulatedWidth)
[m n] = size(InputImage);
A = double(InputImage);

srgr_coef(1) = 836212;
srgr_coef(2) = 0.317727;
srgr_coef(3) = 6.1828e-007;
srgr_coef(4) = -2.76719e-013;
srgr_coef(5) = -6.63693e-021;
srgr_coef(6) = 4.94747e-262;

M_PI = 3.1416;
h = 798769;
r = 6.36828e+006;

mean = sum(sum(A))/(m*n);

multiple = round(SimulatedWidth/n);
pix_spacing = 100*multiple;
for i = 1:m
    for j = 1:n
        %calculate slant range
        RSj = 0;
        for k = 1:6
            RSj = RSj+ srgr_coef(k)*((j-1)*pix_spacing)^(k-1);
        end
    end
end
```

```

        %calculate the angle of incidence
        incidenceAngle = acos((h*h - RSj*RSj + 2*r*h)/(2*r*RSj)) * 180 / M_PI;

        if(incidenceAngle < 20)
            incidenceAngle=20;
        end
        if(incidenceAngle>50)
            incidenceAngle=50;
        end

        %calculate the backscatter
        BS(i,j) = CalculateBS(incidenceAngle);
        Res(i,j) = (A(i,j)+mean)*BS(i,j);
    end
end

%Adjust dynamic range
Result = AdjustDynamicRange(Res);

end

```

```

function backScatter = CalculateBS(incidenceAngle)

SIGMA_MIN = -25;

if(incidenceAngle<=30 && incidenceAngle>=20)
    slope = (4.5-13.5)/(30-20);
    intercept = 13.5;
else
    slope = (13.5-22)/(50-30);
    intercept = -0.75;
end

sigma_0 = incidenceAngle*slope+intercept;

if(sigma_0<SIGMA_MIN)
    sigma_0 = SIGMA_MIN;
end

backScatter = (sigma_0*(-255)/SIGMA_MIN + 255 + 0.5);

```

```
end
```

```
function FinalResult = AddNoise(C, numLooks)
```

```
[rows,cols] = size(C);
```

```
mean_res = sum(sum(C))/(rows*cols);
```

```
C=C+mean_res;
```

```
SumRes = zeros(rows,cols,2);
```

```
%Add illumination variation and speckle noise
```

```
for idx = 1:2
```

```
    for k = 1:numLooks
```

```
        B = zeros(rows,cols);
```

```
        for i = 1:rows
```

```
            for j = 1:cols
```

```
                B(i,j) = C(i,j)*raylrnd(1)*1.37;
```

```
            end
```

```
        end
```

```
        H = zeros(3,3);
```

```
        H(1,2) = 1;
```

```
        H(2,3) = 1;
```

```
        H(2,2) = 4;
```

```
        H = H+H';
```

```
        D = conv2(B,H,'same');
```

```
        % Add phenomenon noise
```

```
        awgn(D,-20,'measured');
```

```
        SumRes(:,:,idx) = SumRes(:,:,idx) + D;
```

```
    end
```

```
    %Average over total number of looks
```

```
    SumRes(:,:,idx) = SumRes(:,:,idx)/numLooks;
```

```
end
```

```
%Account for spatial variation of smoothing filter
```

```
FinRes = zeros(rows,cols);
```

```

for i = 1:rows
    for j = 1:cols
        if(rand(1)<=0.5)
            FinRes(i,j) = SumRes(i,j,1);
        else
            FinRes(i,j) = SumRes(i,j,2);
        end
    end
end

end

FinalResult = AdjustDynamicRange(FinRes);

end

function Res = AdjustDynamicRange(A)
minimum = min(min(A));
maximum = max(max(A));

[m n] = size(A);

for i=1:m
    for j = 1:n
        B(i,j) = (A(i,j)-minimum)*255/(maximum-minimum);
    end
end

Res = uint8(B);
end

```

References

- [1] H.F. Chen, P.N. Belhumeur, and D.W. Jacobs, “In search of illumination invariants,” *Computer Vision and Pattern Recognition, 2000. Proceedings. IEEE Conference on*, vol. 1, pp. 254 –261, 2000.
- [2] Qiyao Yu and D.A. Clausi, “Irgs: Image segmentation using edge penalties and region growing,” *Pattern Analysis and Machine Intelligence, IEEE Transactions on*, vol. 30, no. 12, pp. 2126 –2139, dec. 2008.
- [3] A.K. Qin and D.A. Clausi, “Multivariate image segmentation using semantic region growing with adaptive edge penalty,” *Image Processing, IEEE Transactions on*, vol. 19, no. 8, pp. 2157 –2170, Aug. 2010.
- [4] European Space Agency website, “Geometry glossary,” <http://envisat.esa.int/handbooks/asar/CNTR5-5.htm>.
- [5] J. A. Richards and X. Jia, *Remote Sensing Digital Image Analysis*, 2006.
- [6] R. Bolter, M. Gelautz, and F. Leberl, “Sar speckle simulation,” *International Archives Of Photogrammetry And Remote Sensing*, vol. 31, no. 2, pp. 20 –25, 1996.
- [7] Salim Chitroub, Amrane Houacine, and Boualem Sansal, “Statistical characterisation and modelling of sar images,” *Signal Process.*, vol. 82, pp. 69–92, January 2002.
- [8] Jong-Sen and Lee, “Speckle analysis and smoothing of synthetic aperture radar images,” *Computer Graphics and Image Processing*, vol. 17, no. 1, pp. 24 – 32, 1981.
- [9] Mohammed Shokr, “Compilation of a radar backscatter database of sea ice types and open water using operational analysis of heterogeneous ice regimes,” *Canadian Journal of Remote Sensing*, vol. 35, no. 4, pp. 369–384, 2009.

- [10] B. Scheuchl, R. Caves, D. Flett, and et al., “The Potential of Cross-Polarization Information for Operational Sea Ice Monitoring,” vol. 572, Apr. 2005.
- [11] Peter Yu, “Segmentation of radarsat-2 dual-polarization sea ice imagery,” *MASc. thesis, University of Waterloo*, pp. 1–98, 2009.
- [12] P. Brodatz, *Textures: A Photographic Album*, 1966.
- [13] Robert M. Haralick, K. Shanmugam, and Its’Hak Dinstein, “Textural features for image classification,” *Systems, Man and Cybernetics, IEEE Transactions on*, vol. 3, no. 6, pp. 610 –621, nov. 1973.
- [14] Kenneth R. Castleman, *Digital Image Processing*, Prentice Hall Professional Technical Reference, 1st edition, 1979.
- [15] J. Karvonen, M. Simila, and M. Makynen, “Open water detection from baltic sea ice radarsat-1 sar imagery,” *Geoscience and Remote Sensing Letters, IEEE*, vol. 2, no. 3, pp. 275 – 279, july 2005.
- [16] L.-K. Soh and C. Tsatsoulis, “Texture analysis of sar sea ice imagery using gray level co-occurrence matrices,” *Geoscience and Remote Sensing, IEEE Transactions on*, vol. 37, no. 2, pp. 780 –795, mar 1999.
- [17] S.T. Dokken, B. Haekansson, and J. Askne, “Inter-comparison of arctic sea ice concentration using radarsat, ers, ssm/i and in-situ data,” *Canadian Journal of Remote Sensing*, vol. 26, no. 6, pp. 521–536, 2000.
- [18] J. Karvonen, “C-band sea ice sar classification based on segmentwise edge features,” *Geoscience and Remote Sensing New Achievements*, pp. 129–146, 2010.
- [19] David A. Clausi, “Comparison and fusion of co-occurrence, gabor and mrf texture features for classification of sar sea-ice imagery,” *Atmosphere-Ocean*, vol. 39, pp. 183–194, 2000.
- [20] H.D. Cheng, X.H. Jiang, Y. Sun, and Jingli Wang, “Color image segmentation: advances and prospects,” *Pattern Recognition*, vol. 34, no. 12, pp. 2259 – 2281, 2001.
- [21] Qiyao Yu, “Automated sar sea ice interpretation,” *PhD thesis, University of Waterloo*, pp. 1–159, 2006.

- [22] J. Karvonen and M. Similae, “Pulse-coupled neural network for sea ice SAR image segmentation and classification,” in *Society of Photo-Optical Instrumentation Engineers (SPIE) Conference Series*, T. Lindblad, M. L. Padgett, & J. M. Kinser, Ed., Mar. 1999, vol. 3728 of *Society of Photo-Optical Instrumentation Engineers (SPIE) Conference Series*, pp. 333–350.
- [23] Jorg Haarpaintner and Stian Solbo, “Automatic ice-ocean discrimination in sar imagery,” *Norut IT-report*, pp. 1–28, 2007.
- [24] Leen kiat Soh, Costas Tsatsoulis, Senior Member, Denise Gineris, and Cheryl Bertoia, “Arktos: An intelligent system for sar sea ice image classification,” *IEEE Trans. Geosci. Remote Sens*, vol. 42, pp. 229–248, 2004.
- [25] Yan Wu, Ming Li, Peng Zhang, Haitao Zong, Ping Xiao, and Chunyan Liu, “Unsupervised multi-class segmentation of sar images using triplet markov fields models based on edge penalty,” *Pattern Recogn. Lett.*, vol. 32, pp. 1532–1540, August 2011.
- [26] E.A. Carvalho, D.M. Ushizima, F.N.S. Medeiros, C.I.O. Martins, R.C.P. Marques, and I.N.S. Oliveira, “Sar imagery segmentation by statistical region growing and hierarchical merging,” *Digital Signal Processing*, vol. 20, no. 5, pp. 1365 – 1378, 2010.
- [27] S. Beucher and F. Meyer, “The morphological approach to segmentation: the watershed transformation,” *In Mathematical Morphology in Image Processing (Ed. E.R. Dougherty)*, pp. 433–481, 1993.
- [28] Amer Dawoud and Anton Netchaev, “Fusion of edge information in markov random fields region growing image segmentation,” in *Image Analysis and Recognition*, Aurlio Campilho and Mohamed Kamel, Eds., vol. 6111 of *Lecture Notes in Computer Science*, pp. 96–104. Springer Berlin / Heidelberg, 2010.
- [29] J.A. Karvonen, “Baltic sea ice sar segmentation and classification using modified pulse-coupled neural networks,” *Geoscience and Remote Sensing, IEEE Transactions on*, vol. 42, no. 7, pp. 1566 – 1574, july 2004.
- [30] David Mumford and Jayant Shah, “Optimal approximations by piecewise smooth functions and associated variational problems,” *Communications on Pure and Applied Mathematics*, vol. 42, no. 5, pp. 577–685, 1989.
- [31] Chunming Li, Fang Li, Chiu-Yen Kao, and Chenyang Xu, “Image segmentation with simultaneous illumination and reflectance estimation: An energy minimization

- approach,” in *Computer Vision, 2009 IEEE 12th International Conference on*, 29 2009-oct. 2 2009, pp. 702 –708.
- [32] Luminita A. Vese, Tony F. Chan, Tony, and F. Chan, “A multiphase level set framework for image segmentation using the mumford and shah model,” *International Journal of Computer Vision*, vol. 50, pp. 271–293, 2002.
- [33] H.-C. Lee and D.R. Cok, “Detecting boundaries in a vector field,” *Signal Processing, IEEE Transactions on*, vol. 39, no. 5, pp. 1181 –1194, may 1991.
- [34] Stuart Geman and Donald Geman, “Stochastic relaxation, gibbs distributions, and the bayesian restoration of images,” *Pattern Analysis and Machine Intelligence, IEEE Transactions on*, vol. PAMI-6, no. 6, pp. 721 –741, nov. 1984.
- [35] D. Johnson, “Segmentation of full-scene sar sea-ice imagery,” pp. 1–30, September 2011.
- [36] E.E. Kuruoglu and J. Zerubia, “Modeling sar images with a generalization of the rayleigh distribution,” *Image Processing, IEEE Transactions on*, vol. 13, no. 4, pp. 527 – 533, April 2004.
- [37] MacDonald Dettwiler, “Radarsat data products specifications,” , no. 3, pp. 44–48, 2000.
- [38] Jong-Sen Lee, Karl Hoppel, and Stephen A. Mango, “Unsupervised estimation of speckle noise in radar images,” *International Journal of Imaging Systems and Technology*, vol. 4, no. 4, pp. 298–305, 1992.
- [39] A. Wong and P. Fieguth, “A new bayesian source separation approach to blind decorrelation of sar data,” in *Geoscience and Remote Sensing Symposium (IGARSS), 2010 IEEE International*, july 2010, pp. 4035 –4038.
- [40] Fabrizio Sebastiani, “Machine learning in automated text categorization,” *ACM Comput. Surv.*, vol. 34, pp. 1–47, March 2002.
- [41] Jong-Sen Lee, “Digital image enhancement and noise filtering by use of local statistics,” *Pattern Analysis and Machine Intelligence, IEEE Transactions on*, vol. PAMI-2, no. 2, pp. 165 –168, march 1980.